

1

1 A Pooled Neuronal Activity Screen Links TMEM50A- 2 Dependent MVB Function to Synaptic Integrity and Remote 3 Memory

4

5 Jianhui Wang,^{1,2}† Meiqi Liu,^{3,4}† Yiming Chen,^{1,2}† Jiancheng Chen,^{3,4}
6 Xin Zhong,^{1,2} Zilong Wang,^{1,2}* Xian Jiang,^{3,4}* Ruilin Tian^{1,2}*

7

8 ¹SUSTech Homeostatic Medicine Institute, Department of Medical
9 Neuroscience, School of Medicine, Southern University of Science
10 and Technology, Shenzhen 518055, China

11 ²Key University Laboratory of Metabolism and Health of
12 Guangdong, Southern University of Science and Technology,
13 Shenzhen 518055, China

14 ³Institute of Neurological and Psychiatric Disorders, Shenzhen Bay
15 Laboratory, Shenzhen 518132, China

¹⁶ ⁴School of Chemical Biology and Biotechnology, Peking University
¹⁷ Shenzhen Graduate School, Shenzhen 518055, China

18 †These authors contributed equally

19 *Correspondence: wangzl6@sustech.edu.cn (Z.W.).

20 jiangxian@szbl.ac.cn (X.J.) and tianrl@sustech.edu.cn (R.T.)

21

22 Abstract

23 While advances in omics profiling have rapidly expanded the catalog
24 of genes associated with brain activity in health and disease,
25 functional annotation has lagged far behind. Here, we establish a
26 high-throughput functional genomics platform that couples the
27 calcium-integrating sensor CaMPARI2 with CRISPRi screening in
28 human iPSC-derived neurons. By converting cumulative neuronal

2

3

29 activity into a stable, flow cytometry-readable signal, this approach
30 enables systematic interrogation of neuronal activity through pooled
31 screening. Using a focused library of memory-associated genes, we
32 recover known regulators and identify TMEM50A, a previously
33 uncharacterized protein, as essential for neuronal activity.
34 TMEM50A forms a complex with LEPROT1 and associates with
35 ESCRT-III machinery on multivesicular bodies (MVBs). TMEM50A
36 loss impairs MVB function, remodels the neuronal surface proteome,
37 reduces synapse density, and alters behavior in mice. This platform
38 enables systematic discovery of neuronal activity regulators and
39 reveals a critical role for TMEM50A-dependent MVB function in
40 maintaining synaptic integrity and behavior.

41

4

5

42 **INTRODUCTION**

43 Neuronal activity is a unique physiological property of neurons,
44 fundamental to their function and tightly regulated to support
45 behavior. Its dysregulation contributes to diverse neurological
46 diseases, including epilepsy¹, neurodegenerative diseases², and
47 neurodevelopmental disorders^{3,4}. Neuronal activity is shaped by the
48 intrinsic excitability of individual neurons and by their synaptic
49 connectivity and strength within neural circuits. Although many key
50 regulators have been identified, including ion channels⁵⁻⁸, synaptic
51 assembly factors⁹ and transcriptional and post-translational
52 modulators^{10,11}, the molecular mechanisms controlling neuronal
53 activity remain incompletely characterized and lack systematic
54 investigation.

55

56 Rapid advances in omics profiling technologies have greatly
57 expanded the scale of candidate gene discovery linked to behavior-
58 associated neuronal activity. For example, single-cell
59 transcriptomics have revealed hundreds to thousands of
60 differentially expressed genes (DEGs) in neurons that are active
61 during learning and memory¹²⁻¹⁵. However, a major challenge is to
62 move beyond expression correlations to pinpoint genes, from these
63 long candidate lists, that causally regulate neuronal activity and
64 behavior, and to define the molecular and cellular mechanisms
65 through which they act.

66

67 Systematic identification of genes regulating neuronal activity has
68 been hindered by the lack of high-throughput screening tools for
69 neuronal activity phenotypes. Patch-clamp electrophysiology

7

70 provides gold-standard measurements but is technically demanding
71 and low-throughput^{16,17}. Voltage and calcium imaging with chemical
72 or genetically encoded probes offer optical readout of neuronal
73 activity but capture transient, dynamic signals that require real-time
74 monitoring with fluorescence microscopy or microplate readers¹⁸⁻²⁰,
75 constraining throughput to low- or medium-scale arrayed formats
76 (Figure 1A).

77

78 CaMPARI (Calcium-Modulated Photoactivatable Ratiometric
79 Integrator) offers an alternative strategy for calcium-based neuronal
80 activity detection²¹⁻²⁴. Unlike real-time calcium indicators, CaMPARI
81 is a calcium integrator, capable of recording cumulative calcium
82 activity over defined time periods. Under conditions of elevated
83 intracellular calcium, coincident illumination with violet light
84 induces irreversible photoconversion of CaMPARI from green to red
85 fluorescence. This property enables the conversion of neuronal
86 activity—which is accompanied by Ca^{2+} influx—during a defined
87 illumination window into a stable, integrated fluorescence
88 parameter: the red-to-green (R/G) ratio. CaMPARI has thus been
89 adopted for *in vivo* labeling of behaviorally relevant neuronal
90 ensembles^{25,26}.

91

92 Here, we leveraged CaMPARI's unique ability to convert cumulative
93 neuronal activity into a single, stable fluorescence parameter and
94 coupled it with fluorescence-activated cell sorting (FACS),
95 establishing a high-throughput method for detecting neuronal
96 activity at single-cell resolution (Figure 1A). We further integrated
97 this activity-based sorting approach with a CRISPRi genetic

9

98 screening platform in human induced pluripotent stem cell (iPSC)-
99 derived neurons (iNeurons)²⁷ , developing a pooled high-throughput
100 screening method for neuronal activity. As a proof-of-principle, we
101 applied our CaMPARI-CRISPRi platform to screen a group of DEGs
102 identified via single-cell RNA sequencing (scRNA-seq) during long-
103 term memory formation¹³ . Our screen uncovered both known and
104 previously uncharacterized modulators of neuronal activity. Notably,
105 we identify *TMEM50A*, a gene of previously unknown function, as an
106 essential factor for neuronal activity that acts by controlling
107 multivesicular body (MVB) formation. Loss of *TMEM50A* reduces
108 synapse density, disrupts neuronal electrophysiological properties,
109 and alters behavior in mice, including deficits in remote memory.

110

111 **RESULTS**

112 **Establishing a CaMPARI2-based high-throughput method to** 113 **quantify neuronal activity in human iNeurons**

114 The Ca^{2+} -dependent, irreversible photoconversion of CaMPARI
115 converts transient neuronal activity into a stable fluorescence
116 readout, quantified as the red-to-green (R/G) ratio. This enables
117 cumulative neuronal activity to be measured post hoc in a high-
118 throughput, scalable manner by flow cytometry: for a fixed
119 illumination window, a higher CaMPARI R/G ratio indicates greater
120 Ca^{2+} accumulation and therefore stronger neuronal activity (Figure
121 1A).

122

123 To enable pooled CRISPR screens of neuronal activity, we integrated
124 CaMPARI into our previously developed CRISPRi screening platform
125 in human iNeurons. We introduced CaMPARI2, an improved version

10

11

126 of CaMPARI, via lentiviral infection into iPSCs harboring
127 doxycycline-inducible NGN2 cassette in the AAVS1 safe harbor locus
128 and CRISPRi machinery (dCas9-BFP-KRAB) cassette in the CLYBL
129 locus²⁸ (Figure 1B). Upon NGN2 induction, iPSCs rapidly
130 differentiate into glutamatergic neurons²⁹. These iNeurons are
131 functional excitatory neurons that form excitatory synapses and
132 exhibit robust spontaneous and evoked activity, with
133 electrophysiological properties reaching a steady state at 4-6 weeks
134³⁰.

135

136 Consistent with prior characterization, RNA-seq analysis of our
137 iNeurons at different stages of differentiation (days 14, 21, 28, and
138 35) revealed marked upregulation of genes associated with neuronal
139 activity—including ion channels, glutamate receptors, vesicle
140 release machinery, and synapse formation—after day 14, plateauing
141 at days 21-28 (Figure 1C). Whole-cell patch-clamp recordings of
142 spontaneous and current injection-evoked action potential firing
143 further confirmed that day-28 iNeurons exhibit robust neuronal
144 activity (Figure 1D). We therefore used day-28 iNeurons in
145 subsequent experiments.

146

147 We next characterized whether CaMPARI2 can reliably detect
148 neuronal activity in iNeurons. Using fluorescence microscopy, we
149 observed robust photoconversion in CaMPARI2-iNeurons
150 illuminated with violet light for 5 min (Figure 1E). Importantly, this
151 photoconversion was readily quantified by flow cytometry, with the
152 R/G intensity ratio increasing as a function of illumination time over
153 the 0-10 min range. To ensure sufficient signal while minimizing

12

13

154 light-induced cytotoxicity, we used 5 min of illumination in
155 subsequent experiments.

156

157 We then tested whether CaMPARI2 captures neuronal activity
158 changes. Glutamate stimulation of iNeurons elicited a dose-
159 dependent increase in CaMPARI2 photoconversion, demonstrating
160 that CaMPARI2 reliably reports neuronal activity in response to
161 excitatory input (Figure 1G). To determine whether CaMPARI2 can
162 also detect genetically driven activity modulation, we performed
163 CRISPRi knockdown of two established regulators of neuronal
164 excitability and synaptic function: *TSC1*³¹, a key negative regulator
165 of mTOR signaling implicated in epilepsy and neurodevelopmental
166 disorders, and *STXBP1*²⁹, which encodes a presynaptic vesicle
167 release factor and is associated with developmental and epileptic
168 encephalopathy³². Consistent with reports of decreased activity
169 associated with loss of these genes, flow cytometry revealed reduced
170 CaMPARI2 R/G ratios under both 1-min and 5-min illumination
171 following knockdown of either *TSC1* or *STXBP1* in iNeurons (Figure
172 1H). Collectively, these data establish CaMPARI2 photoconversion
173 as a robust, scalable, flow cytometry-compatible readout for
174 quantifying neuronal activity in human iNeurons.

175

176 **A CaMPARI2-based CRISPRi screen uncovers known and novel**
177 **neuronal activity regulators**

178 Next, we conducted a proof-of-principle CaMPARI2-based neuronal
179 activity screen in iNeurons. To maximize the chance of identifying
180 key regulators, we constructed a biologically informed sgRNA
181 library targeting a set of high-confidence remote-memory-associated

14

15

182 DEGs in excitatory neurons identified in a recent scRNA-seq
183 study¹³. These memory-associated genes reflect stable, long-lasting
184 transcriptional programs linked to remote memory storage and are
185 enriched for pathways involved in synaptic function, neuronal
186 excitability, and activity-dependent plasticity. The sgRNA library
187 comprised 320 sgRNAs targeting 64 genes (5 sgRNAs per gene),
188 alongside 28 non-targeting control sgRNAs (Figure 2A, Table S1).
189 The library was delivered into CaMPARI2-expressing CRISPRi-iPSCs
190 via lentiviral infection, followed by selection, expansion, and
191 differentiation. At Day 28, neurons were illuminated with violet light
192 for 5 min to induce activity dependent CaMPARI2 photoconversion.
193 Subsequently, neurons were sorted by FACS into populations with
194 the highest 30% or lowest 30% R/G ratios. Next-generation
195 sequencing (NGS) was then used to quantify sgRNA representation
196 in each population, and hits were called using the MAGeCK-iNC
197 pipeline^{27,33}.

198

199 The screen uncovered both positive and negative hits, whose
200 knockdown increased or decreased CaMPARI2 signal respectively
201 (Figure 2B, Table S2). Among the hits, we recovered multiple genes
202 previously implicated in synaptic function, intrinsic excitability, or
203 epilepsy³⁴, including *ATP6V0C*³⁵, *HNRNPH2*³⁶, *NSF*³⁷, *STX1B*³⁸,
204 *NCDN*³⁹, *GSK3B*⁴⁰, *PAK1*⁴¹, *SDHA*⁴², *VAMP2*⁴³, *PIGQ*⁴⁴, and
205 *ALG2*³⁴, validating the reliability of our screening strategy.

206

207 Interestingly, among the negative hits we identified *TMEM50A*, a
208 putative transmembrane protein with previously uncharacterized
209 function (Figure 2B), and therefore prioritized it for follow-up. To

16

17

210 confirm the *TMEM50A* phenotype and rule out potential sgRNA off-
211 target effects, we individually cloned three independent sgRNAs
212 targeting *TMEM50A*. Knockdown of *TMEM50A* with each of the
213 three sgRNAs in iNeurons significantly reduced CaMPARI2
214 photoconversion compared to non-targeting controls (Figure 2C,
215 S2A), thereby validating the screening result, and excluding off-
216 target effects.

217

218 To determine whether the reduction in CaMPARI2 signal reflected
219 bona fide changes in neuronal activity, we generated *TMEM50A*
220 knockout (KO) iPSCs (Figure S2B-C) and assessed the
221 electrophysiological properties of the derived iNeurons using whole-
222 cell patch-clamp. Voltage-clamp recordings revealed a significant
223 reduction in both sEPSC frequency and amplitude in *TMEM50A* KO
224 iNeurons, indicating a marked impairment in synaptic transmission
225 (Figure 2D-E). Additionally, current-clamp analysis showed that
226 *TMEM50A* KO iNeurons exhibited a significant reduction in the
227 number of action potentials generated in response to depolarizing
228 current steps compared to controls (Figure 2F-G), indicating
229 reduced intrinsic excitability. Together, these data demonstrate that
230 *TMEM50A* is critical for maintaining neuronal activity levels by
231 supporting both excitatory synaptic drive and intrinsic neuronal
232 responsiveness.

233

234 In summary, our CaMPARI2-based CRISPRi screen provides a robust
235 approach for identifying neuronal activity regulators and identifies
236 *TMEM50A* as a novel factor required to maintain normal neuronal
237 activity in human iNeurons.

18

19

238

239 **TMEM50A localizes to multivesicular bodies**

240 TMEM50A is predicted to encode a four-pass transmembrane
241 protein (Figure S1A) and is highly conserved across vertebrates
242 (Figure S1B). *TMEM50A* has a paralog in the human genome,
243 TMEM50B; however, *TMEM50A* is the predominant paralog
244 expressed in iNeurons, with consistently higher expression than
245 *TMEM50B* across differentiation stages (Figure S1C).

246

247 To begin elucidating how TMEM50A regulates neuronal activity, we
248 first determined its subcellular localization. Because of the lack of
249 suitable antibodies, we initially examined its localization using a
250 fluorescently tagged TMEM50A construct (TMEM50A-HA-GFP) in
251 COS7 cells. However, we found that the expression level of
252 exogenous TMEM50A profoundly affect its localization: transient
253 overexpression produced prominent co-localization with the ER
254 marker Sec61B⁴⁵, whereas lower-level expression via lentiviral
255 transduction reduced the reticular ER signal and revealed a
256 punctate, vesicle-like distribution (Figure S3A). Live-cell imaging
257 further showed that these vesicles were motile and moved along the
258 ER network (Movie S1).

259

260 To determine the localization of endogenous TMEM50A, we
261 generated C-terminal 3×FLAG-mNeonGreen knock-in (KI) lines
262 using CRISPR/Cas9-mediated homology-directed repair (HDR) in
263 both HEK293T cells and iPSCs (Figure S3B). Using super-resolution
264 structured illumination microscopy (SIM), we observed

20

21

265 predominantly vesicular localization of TMEM50A in both HEK293T
266 KI cells and iNeurons derived from the iPSC KI line. In iNeurons,
267 TMEM50A-positive vesicles were detected in both soma and neurites
268 (Figure 3B-C; Movies S2-S4).

269

270 To define the identity of these vesicles, we performed co-localization
271 analysis with markers of distinct membrane compartments⁴⁶,
272 including mRuby-RAB1A (ERGIC), mRuby-RAB5A (early endosome),
273 mRuby-RAB7A (late endosome), mRuby-RAB11A (recycling
274 endosome), and LAMP1 (lysosome). TMEM50A showed predominant
275 co-localization with endosomal markers but not lysosomes (Figure
276 S3C-D).

277

278 We next performed interactome profiling by immunoprecipitation-
279 mass spectrometry (IP-MS) using FLAG pull-down from TMEM50A-
280 3×FLAG-mNeonGreen knock-in iNeurons, with IgG pull-down as a
281 control (Figure 3D; Table S3). Notably, many TMEM50A interactors
282 are involved in vesicular trafficking, including AP2B1⁴⁷, AP2M1⁴⁸,
283 AP2S1⁴⁹, AP2A2⁴⁷, RAB11B^{46,50}, TMEM87A⁵¹, PIK3R4⁵², and
284 VPS51⁵³. In addition, several ESCRT/MVB-related factors were
285 identified, including CHMP7⁵⁴, CHMP1B⁵⁴, CHMP4B⁵⁴, VTA1⁵⁵,
286 and HGS⁵⁶. Gene Ontology analysis further highlighted enrichment
287 for MVB-related pathways (Figure 3E). Consistent with these
288 proteomic data, co-localization analysis with the MVB marker CD63
289 confirmed that TMEM50A is enriched on MVBs (Figure 3F).

290

291 **TMEM50A forms a complex with LEPROT1 and interacts with**

22

23

292 **ESCRT-III to maintain MVB function**

293 Among the TMEM50A interactors identified by IP-MS, LEPROT1
294 emerged as a particularly interesting candidate. Although
295 LEPROT1 function in mammalian cells remains poorly
296 characterized, its yeast homolog Vps55 has been reported to interact
297 with Vps68, the yeast homolog of TMEM50A^{57,58}. AlphaFold3-based
298 structural modeling revealed that yeast Vps55, Vps68, and the
299 Vps55-Vps68 complex closely resemble human LEPROT1,
300 TMEM50A, and the LEPROT1-TMEM50A complex, respectively,
301 with RMSD values of 1.03 Å, 3.44 Å, and 1.25 Å (Figure 4A).

302

303 To determine whether TMEM50A forms a similar complex with
304 LEPROT1 in mammalian cells, we performed co-
305 immunoprecipitation (co-IP) experiments, which demonstrated a
306 robust association between TMEM50A and LEPROT1 (Figure 4B).
307 Consistently, immunofluorescence analysis revealed strong co-
308 localization of TMEM50A and LEPROT1 (Figure 4C-D).
309 Functionally, LEPROT1 knockdown reduced neuronal activity to a
310 similar extent as TMEM50A knockdown as measured by CaMPARI2,
311 and simultaneous knockdown of both genes did not further enhance
312 the phenotype relative to either single knockdown (Figure 4E;
313 Figure 2C), indicating that TMEM50A and LEPROT1 act in the
314 same pathway as a functional complex.

315

316 Multiple ESCRT-III components, including CHMP1B, CHMP4B, and
317 CHMP7, were also identified as TMEM50A interactors (Figure 3B).
318 Co-IP assays further confirmed interactions among TMEM50A,
319 LEPROT1, and CHMP4B (Figure 4F-G). Given the central role of

24

25

320 ESCRT-III in MVB biogenesis, we asked whether the TMEM50A-
321 LEPROT1 complex localizes with ESCRT-III on MVBs. Using
322 TMEM50A-mNeonGreen and LEPROT1-mRuby double knock-in
323 cells, we observed substantial co-localization of TMEM50A and
324 LEPROT1 with CHMP4B and the MVB marker CD63 (Figure 4H).

325

326 Based on these observations, we hypothesized that the TMEM50A-
327 LEPROT1 complex supports MVB function via ESCRT-III. To test
328 this, we performed an EGFR degradation assay, in which ligand-
329 stimulated EGFR is sorted into MVB intraluminal vesicles and
330 subsequently delivered to lysosomes for degradation⁵⁹ (Figure 4I).
331 Notably, *TMEM50A* knockout significantly delayed EGFR
332 degradation compared to control cells (Figure 4J-K), indicating
333 defective MVB-mediated cargo degradation.

334

335 To assess the specificity of this defect, we examined lysosomal
336 integrity using LysoTracker and retrograde transport using cholera
337 toxin B (CTxB) internalization. Neither assay revealed detectable
338 differences between *TMEM50A* knockdown and control cells (Figure
339 S4A-D).

340

341 ESCRT complexes drive intraluminal vesicle formation during MVB
342 biogenesis through membrane remodeling and scission⁶⁰⁻⁶². To
343 determine the impact of TMEM50A on MVB ultrastructure *in vivo*,
344 we performed scanning electron microscopy (SEM) on anterior
345 cingulate cortex (ACC) sections from *Tmem50a*-KO mice.
346 Ultrastructural analysis revealed a marked reduction in the number

26

27

347 of ILVs within MVBs in *Tmem50a*-KO mice compared with WT
348 controls (Figure 4L-M). This phenotype is consistent with defects
349 observed upon ESCRT loss⁶³, further supporting a role for
350 TMEM50A in ESCRT-dependent intraluminal vesicle formation
351 during MVB biogenesis.

352

353 In summary, TMEM50A forms a complex with LEPROTL1 that
354 associates with ESCRT-III at MVBs and is required for efficient
355 ESCRT-dependent intraluminal vesicle formation and MVB-mediated
356 cargo degradation.

357

358 ***TMEM50A* loss remodels neuron surface proteome and
359 reduces synapse density**

360 Because MVBs play a central role in plasma membrane protein
361 turnover^{64,65}, we performed cell-surface biotinylation and affinity
362 purification in WT and *TMEM50A* KO iNeurons, followed by
363 quantitative proteomics to measure changes in surface protein
364 abundance (Figure 5A). *TMEM50A* KO neurons showed widespread
365 alterations in the abundance of plasma membrane proteins (Figure
366 5B, Table S4). Gene ontology analysis of the altered surface
367 proteome revealed enrichment for pathways related to cell-cell
368 adhesion, axon guidance, and synapse organization (Figure 5C).
369 Given the synaptic transmission defects observed in *TMEM50A* KO
370 iNeurons (Figure 2), we next asked whether synapse organization is
371 impaired. Immunostaining for the presynaptic marker Synapsin1/2,
372 the postsynaptic marker PSD95 and the dendrite marker MAP2
373 revealed a significant reduction in synaptic density in *TMEM50A* KO
374 iNeurons. In contrast, puncta size, dendrite number, and soma size

28

29

375 showed no significant changes (Figure 5D-E, S5A).

376

377 We also used mouse primary neurons to validate these findings. We
378 isolated primary cortical neurons from CRISPRi transgenic mice
379 expressing the dCas9-KRAB machinery and infected them with
380 either a control sgRNA or a *Tmem50a*-targeting sgRNA via AAV
381 (Figure 6A). RT-qPCR confirmed a strong reduction of *Tmem50a*
382 mRNA in neurons transduced with the *Tmem50a* sgRNA (Figure 6B).
383 Immunofluorescence analysis revealed synaptic phenotypes
384 consistent with those observed in human iNeurons, showing a
385 significant reduction in synaptic density, while puncta size, dendrite
386 number, and soma size remained unchanged (Figure 6C-D, S5B).

387

388 To assess synaptic alterations *in vivo*, we analyzed synaptic
389 ultrastructure from the SEM images of ACC sections from *Tmem50a*-
390 KO mice. We quantified synaptic cleft width, the number of synaptic
391 vesicles (SVs) per bouton, and postsynaptic density (PSD) length at
392 both inhibitory and excitatory synapses. None of these
393 ultrastructural parameters differed significantly between *Tmem50a*-
394 KO and WT mice (Figure 6E-F). In contrast, synapse density was
395 significantly reduced in *Tmem50a* -KO mice (Figure 6E-F),
396 consistent with the reduced synaptic puncta observed in cultured
397 neurons.

398

399 In summary, TMEM50A loss causes broad remodeling of the
400 neuronal surface proteome and leads to a reduction in synapse
401 density.

30

31

402

403 ***Tmem50a* loss alters memory- and anxiety-related behaviors**
404 **in mice**

405 Given that *TMEM50A* loss impairs neuronal activity, we asked
406 whether it also affects behavior in mice. We first assessed contextual
407 fear memory using a standard fear-conditioning paradigm (Figure
408 7A). *Tmem50a*-KO mice exhibited freezing behavior comparable to
409 WT controls during recent memory retrieval (Day 5), indicating
410 intact recent memory (Figure 7B). In contrast, during remote
411 memory retrieval (Day 21), *Tmem50a*-KO mice displayed
412 significantly reduced freezing compared with WT mice, indicative of
413 impaired remote memory consolidation (Figure 7B).

414

415 We next performed the open field test (Figure 7C). *Tmem50a*-KO
416 mice spent significantly more time in the center of the arena than WT
417 mice, suggesting reduced anxiety-like behavior. Total distance
418 traveled did not differ between *Tmem50a*-KO and WT mice,
419 indicating that this effect was not attributable to altered general
420 locomotor activity.

421

422 Finally, we assessed motor coordination using the rotarod test
423 (Figure 7D). *Tmem50a*-KO and WT mice showed no differences in
424 latency to fall or speed at the time of fall, indicating that *Tmem50a*
425 loss does not impair motor coordination or balance.

426

427 **DISCUSSION**

428 Transcriptomic and genomic studies have generated extensive

32

33

429 catalogs of genes associated with brain activity and behavior in
430 health and disease^{10,17,66}. Yet functional characterization of these
431 candidates has lagged far behind discovery. Here, we begin to
432 address this gap by developing a high-throughput functional
433 genomics platform that couples the calcium-integrating sensor
434 CaMPARI2 with pooled CRISPRi screening in human iPSC-derived
435 neurons. By converting cumulative neuronal activity into a stable,
436 flow cytometry-readable signal, this system enables fluorescence-
437 based sorting of large neuronal populations by activity state, thereby
438 supporting unbiased pooled genetic screens to identify regulators of
439 neuronal activity at scale.

440

441 Compared with patch-clamp electrophysiology and voltage or
442 calcium imaging for detecting neuronal activity, CaMPARI offers a
443 distinct advantage as a calcium recorder: activity is integrated over
444 time and captured as a stable signal that can be measured after
445 stimulation without continuous imaging. While CaMPARI was
446 originally developed to label active neuronal ensembles *in vivo*, we
447 demonstrate that it can quantitatively detect changes in neuronal
448 activity induced by chemical stimulation or genetic perturbations
449 when coupled with flow cytometry.

450

451 CRISPR-based functional genomics has emerged as a powerful
452 approach for systematically interrogating gene function and has
453 been established in neuronal models. Most existing screens in
454 neurons have focused on relatively simple phenotypes, such as cell
455 survival. In this study, we extend CRISPR screening to a complex,
456 neuron-specific phenotype—neuronal activity—thereby broadening

34

35

457 the scope of CRISPR-based functional genomics in neuronal systems.

458

459 As a proof of principle, we screened a focused library of memory-
460 associated DEGs. The screen recovered established regulators of
461 synaptic function and excitability—including *NCDN*³⁹, *STX1B*⁶⁷, and
462 *GSK3B*⁴⁰. The screen also uncovered previously uncharacterized
463 candidates, among which we selected *TMEM50A* for further
464 validation and characterization. *TMEM50A* encodes a predicted
465 four-pass transmembrane protein of unknown function in
466 mammalian cells. Its yeast ortholog, Vps68, interacts with Vps55
467 (the yeast homolog of LEPROL1) and with ESCRT-III components,
468 and has been implicated in vacuolar protein sorting^{57,68}. Our data
469 indicate that these interactions are conserved in mammalian cells:
470 using IP-MS, co-immunoprecipitation, and super-resolution imaging,
471 we demonstrate that TMEM50A forms a complex with LEPROL1
472 that localizes to MVBs and associates with the ESCRT-III component
473 CHMP4B. Functionally, TMEM50A is required for efficient
474 intraluminal vesicle formation and MVB-mediated cargo
475 degradation.

476

477 The ESCRT/MVB pathway is central to plasma membrane protein
478 turnover and has been increasingly implicated in neurological
479 disease, including neurodegeneration and synaptopathies⁶⁹⁻⁷¹.
480 Consistent with these roles, we show that TMEM50A loss broadly
481 remodels the neuronal surface proteome, reduces synapse density,
482 diminishes synaptic transmission and intrinsic excitability, and leads
483 to behavioral phenotypes including impaired remote memory and
484 altered anxiety-like behavior.

36

37

485

486 **Limitations and future directions**

487 First, our proof-of-principle screen used a small, focused library.
488 Given the scalability of our platform, it can be readily extended to
489 larger, even genome-wide, libraries in future studies to achieve a
490 more systematic and comprehensive identification of genes
491 regulating neuronal activity. Additionally, this platform can be
492 adapted to interrogate neuronal activity across diverse contexts.
493 Indeed, while this manuscript was in preparation, a study utilizing a
494 conceptually similar strategy reported screens for regulators of
495 neuronal excitability under glutamate-evoked conditions,
496 highlighting the broad applicability of pooled activity screening⁷².

497

498 Second, our screen was performed in NGN2-induced human
499 iNeurons in 2D culture. Although human iNeurons provide a
500 tractable and reproducible system, they do not fully recapitulate the
501 complexity of the brain environment. Extending this system to more
502 complex models—such as brain organoids, assembloids, or *in vivo*
503 settings—will enable screening in more physiologically relevant
504 contexts. Furthermore, applying this platform to disease contexts,
505 such as patient-derived iNeurons, could enable identification of
506 genetic modifiers that rescue pathological neuronal activity, leading
507 to the discovery of potential therapeutic targets.

508

509 Third, while we demonstrate that TMEM50A interacts with
510 LEPROTL1 and CHMP4B to regulate MVB function, the precise
511 molecular mechanism remains to be defined. Future structural

38

39

512 analysis and biochemical reconstitution studies will be required to
513 elucidate how the TMEM50A-LEPROTL1 complex physically
514 engages ESCRT-III machinery to facilitate membrane remodeling
515 and intraluminal vesicle biogenesis.

516

40

41

517 **MATERIALS AND METHODS**

518 **Cell Culture**

519 ***Cell lines***

520 HEK293T and COS-7 cells (ATCC) were cultured in DMEM (Gibco,
521 C11995500BT) supplemented with 10% FBS (TransGen Biotech,
522 FS301-02) and 1% penicillin-streptomycin (Aladdin, P301861) at
523 37 °C in a humidified incubator with 5% CO₂. Cells were passaged
524 every 2-3 d at a 1:4-1:8 split ratio using 0.05% trypsin-EDTA
525 (Yeasen, 40127ES60).

526

527 ***hiPSC culture and iNeuron differentiation***

528 hiPSCs harboring dCas9-BFP-KRAB and tet-on NGN2 (WTc11
529 background; Coriell GM29371) were maintained in StemFlex
530 medium (Thermo Fisher Scientific, A3349401) on growth factor-
531 reduced, phenol red-free, LDEV-free Matrigel (Corning, 356231)
532 diluted 1:200 in DPBS (Invitrogen, C14190500BT). Cultures were
533 maintained at 37 °C with 5% CO₂ and fed the day after seeding and
534 every other day thereafter. For passaging at ~80% confluence, cells
535 were rinsed with DPBS, incubated with Accutase (STEMCELL
536 Technologies, 07922) for 3-5 min at 37 °C, diluted 3-5× with DPBS,
537 gently triturated to single cells, and centrifuged at 200 × g for 5 min
538 at room temperature. Pellets were resuspended in StemFlex
539 supplemented with Y-27632 ROCK inhibitor (Selleck, S1049),
540 counted, and replated onto fresh Matrigel-coated dishes at a 1:6-
541 1:10 split ratio. ROCK inhibitor was maintained for the first 24 h
542 post-passaging and then removed.

543

42

43

544 iNeurons were generated as previously described²⁷. Briefly, hiPSCs
545 were pre-differentiated on Matrigel-coated plates in N2 pre-
546 differentiation medium consisting of KnockOut DMEM/F12, 1×
547 MEM non-essential amino acids, 1× N2 Supplement (Gibco, 17502-
548 048), NT-3 (10 ng/mL; PeproTech, 450-03), BDNF (10 ng/mL;
549 PeproTech, 450-02), mouse laminin (1 µg/mL; Thermo Fisher
550 Scientific, 23017-015), ROCK inhibitor (10 nM), and doxycycline (2
551 µg/mL) to induce mNGN2 expression. After 3 d, cells were replated
552 (designated Day 0) onto plates coated with 0.1% PEI and laminin in
553 neuronal medium containing a 1:1 mixture of DMEM/F12 (Gibco,
554 11320-033) and Neurobasal-A (Gibco, 10888-022), 1× MEM non-
555 essential amino acids, 0.5× GlutaMAX (Gibco, 35050-061), 0.5× N2
556 Supplement, 0.5× B27 Supplement (Gibco, 17504-044), NT-3 (10
557 ng/mL), and BDNF (10 ng/mL). Half medium was replaced weekly.

558

559 ***Primary mouse neuron culture***

560 Primary cortical neurons were prepared from embryonic mice (E14-
561 E18) as previously described with minor modifications⁷³. Cortices
562 were dissociated with 0.25% trypsin-EDTA (Gibco, 25200072) for 10
563 min at 37 °C, followed by trituration using a Pasteur pipette.
564 Digestion was terminated with DMEM/F12 (Gibco, C11330500BT)
565 supplemented with 10% FBS (Gibco, A5669701), and DNase I was
566 added to reduce aggregation. Dissociated neurons were plated onto
567 poly-D-lysine-coated glass coverslips (Beyotime, ST508) in 24-well
568 plates and maintained in Neurobasal medium (Thermo Fisher
569 Scientific, 10888022) supplemented with 2% B27 (Gibco, 17504044)
570 and 0.5% GlutaMAX (Gibco, 35050061) at 37 °C with 5% CO₂.

571

44

45

572 ***Mycoplasma testing***

573 Mycoplasma contamination was routinely screened by PCR, and all
574 cultures were confirmed mycoplasma-free.

575

576 **Mice**

577 *Tmem50a*-KO mice (C57BL/6JCya-Tmem50aem1) were purchased
578 from Cyagen. This line carries a conventional *Tmem50a* knockout
579 allele generated by CRISPR/Cas9-mediated deletion (NCBI Gene ID:
580 71817). Two guide RNAs targeting exon regions were used:
581 CTTAAGAACATATGTCAGA and AAAATTCCCAGCCCTGGGT.
582 CRISPRi mice (H11^{dCas9-KRAB}) were purchased from The Jackson
583 Laboratory (#030000). These mice express a catalytically inactive
584 Cas9 fused to the KRAB repressor, inserted into the H11 locus of the
585 mouse genome by targeted knock-in. C57BL/6 wild-type mice were
586 obtained from Guangdong Medical Laboratory Animal Center. All
587 mice were group-housed (maximum 5 per cage) in a specific-
588 pathogen-free (SPF) environment. They were maintained on a 12 h
589 light-dark cycle (lights on 08:00-20:00) with ad libitum access to
590 food and water. Male mice aged 6-8 weeks were used for all
591 experiments. All surgical procedures were performed under
592 isoflurane or tribromoethanol anesthesia, and every effort was made
593 to minimize pain and distress. All animal experimental procedures
594 were approved by the Animal Care and Use Committee at Shenzhen
595 Bay Laboratory (AEJX20220201A) and Shenzhen Medical Academy
596 of Research and Translation (SMART-IACUC-2025-A023) and
597 conducted in accordance with institutional guidelines.

598

599 **Lentiviral production**

46

47

600 HEK293T cells were seeded the day prior at ~30% density and
601 allowed to reach ~70–80% confluence on the day of transfection. For
602 small-scale lentiviral packaging in 6-well plates, 1 µg transfer
603 plasmid and 1 µg third-generation packaging mix were diluted in 200
604 µL Opti-MEM and combined with 6 µg PEI (Yeasen, 40816ES01) for
605 each well. For large-scale packaging of sgRNA library, one 15-cm
606 dish was used with 15 µg packaging plasmid and 15 µg library
607 plasmid diluted in 2 mL Opti-MEM with 90 µg PEI. The transfection
608 mixture was incubated at room temperature for 15 min and then
609 added to the cells. At 48 h post-transfection, supernatants were
610 collected, passed through a 0.45 µm PVDF syringe filter into conical
611 tubes, mixed with ¼ volume lentiviral pellet solution, and held at 4
612 °C for 24 h. Virus-containing supernatants were centrifuged at 3,500
613 × g for 30 min at 4 °C, the supernatant was aspirated, and a brief
614 clarification spin (3,500 × g, 2 min, 4 °C) was performed. Pellets
615 were resuspended in DPBS, aliquoted, and stored at –80 °C.

616

617 **AAV production and transduction of primary neuron**

618 Recombinant adeno-associated viruses (AAVs) were packaged at a
619 titer of 1×10^{12} by Institute of Molecular Physiology, Shenzhen Bay
620 Laboratory. Primary cortical neurons were transduced at day in vitro
621 4 (DIV4), with control and experimental viruses applied at
622 comparable titers.

623

624 **CaMPARI2 photoconversion assay**

625 The CaMPARI2 cassette (Addgene #101060) was subcloned into a
626 lentiviral vector containing a CAG promoter and an upstream UCOE
627 element via Gibson assembly. A stable CaMPARI2 hiPSC line was

49

628 generated by lentiviral transduction of hiPSCs harboring
629 dCas9-BFP-KRAB and tet-on NGN2.

630

631 Photoconversion was induced by 405-nm LED illumination of Day 28
632 CaMPARI2 iNeurons and quantified by confocal microscopy (Nikon
633 ECLIPSE Ts2) or flow cytometry (BD FACSaria SORP). For flow
634 cytometry, cells were enzymatically dissociated with papain
635 (Worthington, PAP2; 20 U/mL in 1× DPBS) supplemented with
636 DNase I (10 U/mL) for 15 min at 37 °C. Digestion was quenched with
637 3 volumes of DMEM containing 10% FBS, and cells were pelleted
638 (500 × g, 10 min). Pellets were resuspended in DPBS with 5% FBS
639 and analyzed by flow cytometry; data were processed using FlowJo
640 v10.

641

642 **Generation of sgRNA library targeting memory-associated
643 genes**

644 A set of memory-associated genes was derived from a published
645 scRNA-seq study that identified 64 remote-memory-associated DEGs
646 in excitatory neurons¹³. For each gene, the top five sgRNAs were
647 selected from the CRISPRi-v2 library (ref), and 28 non-targeting
648 control sgRNAs were included, yielding a final library of 348 sgRNAs
649 (Table S1). An sgRNA oligonucleotide pool was synthesized
650 (GENEWIZ) and cloned into pCRISPRia-v2 (Addgene #84832) using
651 the BstXI and BpuI restriction sites. To assess library quality, the
652 sgRNA-containing region was PCR-amplified using Phanta Flash
653 Master Mix (Vazyme, P520) according to the manufacturer's
654 instructions, and PCR products were analyzed by next-generation
655 sequencing.

50

51

656

657 **CaMPARI2-based CRISPRi screening**

658 sgRNA library was transduced into hiPSCs via lentiviral infection at
659 a multiplicity of infection (MOI) of ~0.3, followed by puromycin
660 selection. After expansion, hiPSCs were differentiated into iNeurons
661 and plated at 1×10^7 cells per plate onto 10-cm PEI-coated dishes.

662

663 On Day 28, iNeurons were subjected to CaMPARI2 photoconversion
664 followed by papain dissociation. Dissociated neurons were
665 transferred to 15-mL conical tubes and centrifuged at $500 \times g$ for 5
666 min. Pellets were gently resuspended in 2 mL DPBS, passed through
667 a 100- μ m cell strainer to remove axonal debris and incompletely
668 dissociated aggregates, and the filtrate was transferred to flow
669 cytometry tubes for FACS.

670

671 For FACS, cells were first gated by forward and side scatter to select
672 live singlets, then sorted based on the CaMPARI2 red-to-green
673 fluorescence ratio (R/G; green excited at 488 nm and collected at
674 ~530/30 nm, red excited at 561 nm and collected at ~610/20 nm).
675 The top 30% (“high-ratio”) and bottom 30% (“low-ratio”) fractions
676 were collected. Sorted cells were pelleted at $500 \times g$ for 5 min, and
677 genomic DNA was extracted using the TIANamp Genomic DNA Kit
678 (Tiangen, DP304-03) according to the manufacturer’s instructions.
679 sgRNA cassettes were PCR-amplified with adapter primers using
680 Phanta Flash Master Mix (Vazyme, P520) to generate sequencing-
681 ready products. PCR products were purified with Hieff NGS® DNA

52

53

682 Selection Beads V2 (YEASEN, 12418ES08) and subjected to next-
683 generation sequencing.

684

685 The MAGeCK-iNC pipeline was used to evaluate sgRNA- and gene-
686 level phenotypes relative to non-targeting controls³³. Raw
687 sequencing reads were trimmed and aligned using publicly available
688 custom scripts from the Kampmann Lab
689 (<https://kampmannlab.ucsf.edu/resources>). Phenotype scores and p-
690 values for target genes and non-targeting controls were computed
691 using the Mann-Whitney U test. Hit genes were defined using an
692 empirical false discovery rate (FDR) threshold of 0.01 (Table S2).

693

694 **sgRNA cloning**

695 Individual sgRNAs were synthesized and cloned into the pLG15
696 vector using the BstXI and Bpu1102I restriction sites as previously
697 described²⁷. The pLG15 vector contains a mouse U6 promoter
698 driving sgRNA expression, and an EF1 α promoter that drives
699 puromycin resistance cassette and BFP for selection. Constructs
700 were verified by Sanger sequencing. Individual sgRNAs used in this
701 study are listed in Table S5.

702

703 **RNA extraction and quantitative real-time PCR**

704 Total RNA was isolated with the MolPure® Cell RNA Kit (Yeasen,
705 19231ES50) following the manufacturer's instructions. Reverse
706 transcription was carried out using the HiScript III 1st Strand cDNA
707 Synthesis Kit (Vazyme, R312). Quantitative real-time PCR was
708 performed on an FDQ-96A real-time fluorescence detection system

54

55

709 using AceQ qPCR SYBR Green Master Mix (Vazyme, CQ111-02)
710 according to the supplier's protocol. GAPDH served as the
711 endogenous normalization control. Primers used in this study are
712 listed in Table S5.

713

714 **CRISPR-mediated gene knockout**

715 sgRNAs targeting TMEM50A exon 1 were designed using
716 CHOPCHOP⁷⁴ and cloned into pX459 (Addgene #62988). Constructs
717 were verified by Sanger sequencing. hiPSCs were transfected using
718 LipofectamineTM Stem (Invitrogen, STEM00003); HEK293T cells
719 were transfected with PEI (Yeasen, 40816ES01). At 48 h post-
720 transfection, cells were selected with puromycin, recovered for 48 h,
721 and genotyped. Editing efficiency was assessed by ICE (Synthego).
722 For clonal isolation, 250 cells were seeded on Matrigel-coated 35-
723 mm dishes; colonies were manually picked into 48-well plates for
724 expansion and genotyping.

725

726 **CRISPR-mediated endogenous knock-in**

727 An sgRNA targeting the desired knock-in site was cloned into pX459
728 (Addgene #62988). A dsDNA donor containing microhomology arms
729 flanking the cut site, a 3×FLAG tag, and a fluorescent protein
730 cassette was co-transfected using Hieff Trans (Yeasen, 40802ES02)
731 for HEK293T cells or LipofectamineTM Stem (Invitrogen,
732 STEM00003) for hiPSCs. Puromycin (2 µg/mL) was applied 48 h
733 post-transfection for 72 h, followed by recovery. Fluorescent-positive
734 cells were single-cell sorted (BD FACSAria SORP) into 96-well plates
735 (one cell per well). After ~2 weeks, clones were genotyped by PCR
736 and validated by Sanger sequencing.

56

57

737

738 **Electrophysiology**

739 EPSC recording was performed as described previously^{75,76}.
740 Electrodes had a resistance of 4-5 MΩ when filled with the pipette
741 solution, which contained: 140 mM KCl, 0.5 mM EGTA, 5 mM HEPES
742 and 3 mM Mg-ATP (pH 7.4 with KOH). The extracellular solution
743 contained: 140 mM NaCl, 3 mM KCl, 2 mM MgCl₂, 2 mM CaCl₂, 10
744 mM HEPES (pH 7.4 with NaOH). The whole-cell recording
745 configuration was obtained in voltage clamp mode with an EPC-10
746 amplifier (HEKA) at a sampling rate of 20 kHz. For action potential
747 (AP) recording, APs were evoked by a set of stepped increasing
748 currents (-20 to 120 pA, 300 ms; in increments of 10 pA) (PMID:
749 40750771).

750

751 **Immunoprecipitation-Mass Spectrometry (IP-MS)**

752 *TMEM50A* knock-in iNeurons were cultured on twelve 15-cm dishes
753 (3 × 10⁷ cells/dish). On Day 21, neurons were washed twice with ice-
754 cold DPBS and scraped into DPBS. Cells were resuspended in 2 mL
755 lysis buffer and lysed on ice for 30 min with occasional vortexing.
756 Lysates were clarified at 14,000 rpm for 10 min at 4 °C.
757 To 1 mL clarified lysate, 80 µL BeyoMag Anti-FLAG beads (Beyotime,
758 P2115) and 80 µL BeyoMag Mouse IgG beads (Beyotime, P2171)
759 were added and rotated overnight at 4 °C. Beads were collected,
760 washed twice with TBST (TBS + 0.1% Tween-20), and bound
761 proteins were eluted and analyzed by SDS-PAGE followed by MS to
762 identify *TMEM50A* interactors (Table S3).

763

59

764 **Western blot**

765 Cells were collected and washed with cold DPBS. Cells were lysed
766 with lysis buffer (1% DDM, 150 mM HEPES, [pH 7.4], 150 mM NaCl)
767 supplemented with EDTA-free protease inhibitor cocktail (Epizyme,
768 GRF101) on ice for 30 min. The soluble fractions of cell lysates were
769 isolated by centrifugation at 15,000 rpm for 10 min at 4 °C. Proteins
770 were denatured by the addition of 5 × SDS sampling buffer and no
771 boiling. Samples were subjected to SDS-PAGE and immunoblotting
772 analysis.

773

774 **Co-immunoprecipitation (Co-IP)**

775 HEK293T cells were plated on a 10 cm dish for 24 h before
776 transfection with pcDNA3.1-GFP, pcDNA3.1-TMEM50A-GFP,
777 pcDNA3.1-LEPROTL1-myc-mRuby, or pcDNA3.1-CHMP4B-V5-BFP.
778 After 48 h, cells were lysed in lysis buffer, and the lysates were
779 centrifuged at 15,000 rpm for 10 minutes at 4°C. The supernatant
780 was incubated with ABM® Anti-GFP VHH Agarose (ABMagic,
781 MA108) or ABM® Anti-MYC VHH Magarose (ABMagic, MA105) at
782 4°C overnight. After washing, the beads were denatured and
783 analyzed by immunoblotting.

784

785 **EGFR degradation assay**

786 HEK293T cells were seeded at 0.5×10^6 cells per well into five wells
787 of a 12-well plate and incubated for 24 h at 37 °C, 5% CO₂. The
788 medium was then replaced with serum- and antibiotic-free DMEM,
789 and cells were serum-starved overnight. Cells were washed twice
790 with DPBS, then 0.5mL of EGF-containing DMEM (200 ng/ml) was
791 added per well. Plates were incubated at 37 °C, 5% CO₂ for 0, 20, 40,

60

61

792 80, and 120 min. At each time point, medium was aspirated, and cells
793 were detached with trypsin, collected, and centrifuged at $200 \times g$ for
794 5 min. Pellets were washed three times with DPBS and the final
795 pellet was used for lysis. Cells were lysed on ice for 30 min in 100 μL
796 lysis buffer (1% NP-40, 200 mM NaCl, 50 mM Tris-HCl, pH 8.0;
797 optionally supplemented with protease/phosphatase inhibitors).
798 Lysates were clarified, resolved by SDS-PAGE, and analyzed by
799 immunoblotting with antibodies against EGFR (Cell Signaling
800 Technology, 4267S) and GAPDH (Proteintech, HRP-60004).

801

802 **Surface Biotinylation Assay**

803 Cell surface biotinylation was performed using the Pierce™ Cell
804 Surface Protein Biotinylation Kit according to the manufacturer's
805 instructions. WT and *TMEM50A* KO iNeurons were rinsed with DPBS
806 and incubated with 0.125 mg/mL EZ-Link™ Sulfo-NHS-SS-Biotin
807 (membrane-impermeable) in DPBS for 1 h at room temperature. The
808 reaction was quenched with 50 mM glycine for 10 min. Cells were
809 washed three times with ice-cold PBS, harvested, and lysed in 1 mL
810 lysis buffer supplemented with a complete protease inhibitor
811 cocktail. Lysates were clarified by centrifugation at $15,000 \times g$ for 10
812 min at 4 °C, and protein concentrations were determined by BCA
813 assay. A total of 500 μg protein was incubated with 60 μL
814 NeutrAvidin agarose resin (Thermo Scientific) overnight at 4 °C with
815 gentle agitation. Resin was washed three times with TBST, and
816 biotinylated proteins were eluted using the kit elution buffer.

817

818 **Cholera toxin subunit B (CTxB) assay**

62

63

819 CTxB trafficking assay was performed as described previously⁷⁷.
820 HEK293T cells were incubated with cholera toxin subunit B (CTxB;
821 1:1000 in culture medium) for 5 min at 37 °C. Coverslips were
822 washed and chased for 1 h, then cells were washed with PBS and
823 fixed with 4% paraformaldehyde (PFA) for 10 min. Cells were
824 immunostained for the Golgi marker GM130. Retrograde transport
825 of CTxB was quantified by calculating the Pearson's colocalization
826 coefficient between CTxB and GM130 in Fiji (ImageJ, NIH).

827

828 **Immunocytochemistry**

829 The immunocytochemistry experiments were conducted as
830 previously described⁷⁸. Briefly, cultured neurons on DIV14 were
831 fixed with 4% paraformaldehyde (leagene #DF0135), permeabilised
832 with 0.3% Triton X-100(Solarbio #T8200) for 20 minutes and
833 blocked with 5% BSA (Solarbio #A8010) for 30 minutes. Cells were
834 incubated with primary antibodies at 4 °C overnight, followed by
835 incubation with fluorophore-conjugated secondary antibodies at
836 room temperature for 2 hours, and coverslips were mounted using
837 Fluoromount-G (Southern Biotech #0100-01). Images were acquired
838 using a Zeiss LSM900 confocal microscope using identical
839 acquisition settings across conditions. Z-stacks were collected at 0.5
840 mm intervals and maximum-intensity projections were used for
841 quantification. The subsequent primary antibodies were used:
842 Guinea pig anti-MAP2 (1:1000 dilution, SYSY #SYS-188-004), Rabbit
843 anti-MAP2 (1:1000 dilution; SYSY; Cat# 188 002), Chicken anti-
844 synapsin 1/2 (1:500 dilution, SYSY #106006), Mouse anti-PSD95
845 (1:500 dilution, Thermo MA1-046). Secondary antibodies included
846 Goat anti-guinea pig IgG Alexa Fluor™ 647 (Invitrogen#A-21450),
847 Goat anti-mouse IgG Alexa Fluor™ 488 (Abcam #ab150113), Goat

64

65

848 anti-Chicken IgY Alexa Fluor™ 488 (Thermo #A32931). Goat anti-
849 rabbit IgG Alexa Fluor 647 (1:500 dilution; Sangon; Cat# D110078),
850 Goat anti-mouse IgG Alexa Fluor 555 (1:1000 dilution; Thermo; Cat#
851 A-21428), Goat anti-chicken IgG Alexa Fluor 488 (1:500 dilution;
852 Sangon; Cat# D110061).

853

854 **Scanning electron microscopy (SEM)**

855 6-week-old C57BL/6 wild-type (n = 3) and TMEM50A-KO mice (n =
856 3) were used for SEM analysis. Mice were transcardially perfused
857 first with ice-cold phosphate-buffered saline (PBS), followed by ice-
858 cold fixative consisting of 4% paraformaldehyde and 1%
859 glutaraldehyde in 0.1 M phosphate buffer (pH 7.2–7.4). The anterior
860 cingulate cortex (ACC) was dissected using a brain matrix (RWD
861 #68713) and cut into approximately 1 × 1 × 1 mm³ blocks. Tissue
862 samples were further fixed in 2.5% glutaraldehyde at room
863 temperature for 2 h and then overnight at 4 °C. Subsequent sample
864 processing was performed by the Bioimaging Core Facility of
865 Shenzhen Bay Laboratory according to standard protocols. Images
866 were acquired using a Zeiss Gemini 1 360 scanning electron
867 microscope. SEM images were acquired at an accelerating voltage of
868 3.0 kV with a working distance of approximately 5.3 mm using a
869 backscattered electron detector (Volume BSD), at a magnification of
870 10,000× and a resolution of 4,096 × 3,072 pixels.

871

872 **Animal behavior**

873 ***Contextual fear conditioning***

874 Contextual fear conditioning was performed as previously described
875 ¹³. Mice were handled for 3 min per day for three consecutive days

67

876 prior to training. On each experimental day, mice were transferred
877 to the behavioral testing room and allowed to acclimate for at least
878 30 min before the session. Training was conducted in a fear-
879 conditioning chamber (25 × 25 × 25 cm) equipped with a stainless-
880 steel grid floor (Panlab, Harvard Apparatus) and maintained at 23–25
881 °C. All sessions were performed during the dark phase of the
882 light/dark cycle and controlled using FREEZING and STARTLE
883 software (Panlab, Harvard Apparatus). During encoding training,
884 mice were allowed to freely explore the context for 3 min, followed
885 by delivery of three-foot shocks (0.5 mA, 2 s) through the grid floor at
886 180 s, 242 s, and 304 s. Each shock was followed by a 60 s post-shock
887 interval. Mice were removed from the chamber 60 s after the final
888 shock and returned to their home cages. Chambers were thoroughly
889 cleaned by 75% ethanol between animals. For retrieval testing, mice
890 were re-exposed to the same context without shock for a 3-min
891 session either 1 day (recent retrieval) or 16 days (remote retrieval)
892 after training. Freezing behaviour was quantified automatically
893 using the software, defined as immobility below a threshold of 4
894 arbitrary units (AU) for a minimum duration of 500 ms. The
895 percentage of freezing was calculated over the entire 3-min test
896 session.

897

898 ***Open field test***

899 Open field test was conducted as previously described ⁷⁹. Mice were
900 transferred to the behavioral testing room and allowed to acclimate
901 for at least 30 min before the test. Mice were then individually placed
902 in the center of an open field arena (RWD #63008, gray acrylic, 400
903 × 400 × 400 mm) and allowed to explore for 10 min. Total distance
904 and time in central zone was automatically recorded by the

68

69

905 SMARTPREMIUM Panlab Explore system (v3.0). The central zone
906 was defined as a 16 × 16 cm area. Tests were performed under dim
907 conditions (lights off) and maintained at 23–25 °C during the dark
908 phase of the light/dark cycle, and the arena was thoroughly cleaned
909 by 75% ethanol between trials.

910

911 ***Rotarod test***

912 Rotarod tests were performed similarly as previously described⁸⁰.
913 Mice were transferred to the behavioral testing room and allowed to
914 acclimate for at least 30 min before the session. Mice were first
915 trained on the rotating rod at 5 rpm for 3 trials with 10 minutes
916 intervals. Mice were first trained on a rotarod apparatus (Panlab
917 Harvard Apparatus #LE8505, rod length 60 mm) at a constant speed
918 of 5 rpm for three trials, with 10-min inter-trial intervals. Testing was
919 then performed with an initial speed of 4 rpm that accelerated
920 linearly to 40 rpm over 300 s. Each mouse underwent three test trials
921 with 1-h inter-trial intervals, and the time latency to fall and the
922 speed at the time to fall were automatically recorded by the system
923 and the mean was used for analysis. The rod was cleaned thoroughly
924 cleaned by 75% ethanol between animals.

925

926 **QUANTIFICATION AND STATISTICAL ANALYSIS**

927 All data were analyzed using GraphPad Prism 10 (GraphPad
928 Software Inc.). Statistical comparisons between two groups were
929 performed using Student's t test, and comparisons involving three or
930 more groups were performed using one-way or two-way ANOVA with
931 appropriate corrections for multiple comparisons. p values < 0.05,
932 0.01, and 0.001 were considered statistically significant and are

71

933 denoted by *, **, and ***, respectively. Sample sizes and statistical
934 methods for each quantification are provided in the figure legends.
935

72

936 **Reference**

937

938 1. Peters, H.C., Hu, H., Pongs, O., Storm, J.F., and Isbrandt, D. (2005).
939 Conditional transgenic suppression of M channels in mouse brain
940 reveals functions in neuronal excitability, resonance and behavior.
941 Nat. Neurosci. 8, 51-60. <https://doi.org/10.1038/nn1375>.

942 2. Andersen, O.M., Monti, G., Jensen, A.M.G., Waal, M.W.J. de,
943 Hulsman, M., Olsen, J.G., and Holstege, H. (2024). Basic Science and
944 Pathogenesis. Alzheimer's Dement. : J. Alzheimer's Assoc. 20 *Suppl*
945 1, e084835. <https://doi.org/10.1002/alz.084835>.

946 3. Le, S., Menacho, C., and Prigione, A. (2024). Balancing neuronal
947 activity to fight neurodevelopmental disorders. Trends Neurosci. 47,
948 241-242. <https://doi.org/10.1016/j.tins.2024.03.002>.

949 4. Smith, R.S., and Walsh, C.A. (2020). Ion Channel Functions in
950 Early Brain Development. Trends Neurosci. 43, 103-114.
951 <https://doi.org/10.1016/j.tins.2019.12.004>.

952 5. Sun, A.X., Yuan, Q., Fukuda, M., Yu, W., Yan, H., Lim, G.G.Y., Nai,
953 M.H., D'Agostino, G.A., Tran, H.-D., Itahana, Y., et al. (2019).
954 Potassium channel dysfunction in human neuronal models of
955 Angelman syndrome. Science 366, 1486-1492.
956 <https://doi.org/10.1126/science.aav5386>.

957 6. Tyagi, S., Higerd-Rusli, G.P., Akin, E.J., Waxman, S.G., and Dib-
958 Hajj, S.D. (2025). Sculpting excitable membranes: voltage-gated ion
959 channel delivery and distribution. Nat. Rev. Neurosci. 26, 313-332.
960 <https://doi.org/10.1038/s41583-025-00917-2>.

961 7. Shah, M.M., Hammond, R.S., and Hoffman, D.A. (2010). Dendritic
962 ion channel trafficking and plasticity. Trends Neurosci. 33, 307-316.
963 <https://doi.org/10.1016/j.tins.2010.03.002>.

964 8. Imbrici, P., Jaffe, S.L., Eunson, L.H., Davies, N.P., Herd, C.,
965 Robertson, R., Kullmann, D.M., and Hanna, M.G. (2004). Dysfunction
966 of the brain calcium channel CaV2.1 in absence epilepsy and
967 episodic ataxia. Brain 127, 2682-2692.
968 <https://doi.org/10.1093/brain/awh301>.

969 9. Aarts, M., Liu, Y., Liu, L., Besshoh, S., Arundine, M., Gurd, J.W.,
970 Wang, Y.-T., Salter, M.W., and Tymianski, M. (2002). Treatment of

971 Ischemic Brain Damage by Perturbing NMDA Receptor- PSD-95
972 Protein Interactions. Science 298, 846-850.
973 <https://doi.org/10.1126/science.1072873>.

974 10. Yap, E.-L., and Greenberg, M.E. (2018). Activity-Regulated
975 Transcription: Bridging the Gap between Neural Activity and
976 Behavior. Neuron 100, 330-348.
977 <https://doi.org/10.1016/j.neuron.2018.10.013>.

978 11. Das, S., Lituma, P.J., Castillo, P.E., and Singer, R.H. (2023).
979 Maintenance of a short-lived protein required for long-term memory
980 involves cycles of transcription and local translation. Neuron 111,
981 2051-2064.e6. <https://doi.org/10.1016/j.neuron.2023.04.005>.

982 12. Sun, W., Liu, Z., Jiang, X., Chen, M.B., Dong, H., Liu, J., Südhof,
983 T.C., and Quake, S.R. (2024). Spatial transcriptomics reveal neuron-
984 astrocyte synergy in long-term memory. Nature 627, 374-381.
985 <https://doi.org/10.1038/s41586-023-07011-6>.

986 13. Chen, M.B., Jiang, X., Quake, S.R., and Südhof, T.C. (2020).
987 Persistent transcriptional programmes are associated with remote
988 memory. Nature 587, 437-442. <https://doi.org/10.1038/s41586-020-2905-5>.

990 14. Bahl, E., Chatterjee, S., Mukherjee, U., Elsadany, M.,
991 Vanrobaeys, Y., Lin, L.-C., McDonough, M., Resch, J., Giese, K.P.,
992 Abel, T., et al. (2024). Using deep learning to quantify neuronal
993 activation from single-cell and spatial transcriptomic data. Nat.
994 Commun. 15, 779. <https://doi.org/10.1038/s41467-023-44503-5>.

995 15. Yamashita, K., Kinoshita, F.L., Yoshida, S.Y., Matsumoto, K.,
996 Mitani, T.T., Fujishima, H., Minami, Y., Morii, E., Yamada, R.G.,
997 Okada, S., et al. (2025). A whole-brain single-cell atlas of circadian
998 neural activity in mice. Science, eaea3381.
999 <https://doi.org/10.1126/science.aea3381>.

1000 16. Fuzik, J., Zeisel, A., Máté, Z., Calvignoni, D., Yanagawa, Y., Szabó,
1001 G., Linnarsson, S., and Harkany, T. (2016). Integration of
1002 electrophysiological recordings with single-cell RNA-seq data
1003 identifies neuronal subtypes. Nat. Biotechnol. 34, 175-183.
1004 <https://doi.org/10.1038/nbt.3443>.

1005 17. Gao, Y., Dong, Q., Arachchilage, K.H., Risgaard, R.D., Syed, M.,
1006 Sheng, J., Schmidt, D.K., Jin, T., Liu, S., Sandoval, S.O., et al. (2025).

1007 Multimodal analyses reveal genes driving electrophysiological
1008 maturation of neurons in the primate prefrontal cortex. *Neuron*.
1009 <https://doi.org/10.1016/j.neuron.2025.04.025>.

1010 18. Sterin, I., Santos, A.C., and Park, S. (2022). Neuronal Activity
1011 Reporters as Drug Screening Platforms. *Micromachines-basel* *13*,
1012 1500. <https://doi.org/10.3390/mi13091500>.

1013 19. Lee, D., Hyun, J.H., Jung, K., Hannan, P., and Kwon, H.-B. (2017).
1014 A calcium- and light-gated switch to induce gene expression in
1015 activated neurons. *Nat. Biotechnol.* *35*, 858-863.
1016 <https://doi.org/10.1038/nbt.3902>.

1017 20. Grienberger, C., and Konnerth, A. (2012). Imaging Calcium in
1018 Neurons. *Neuron* *73*, 862-885.
1019 <https://doi.org/10.1016/j.neuron.2012.02.011>.

1020 21. Fosque, B.F., Sun, Y., Dana, H., Yang, C.-T., Ohyama, T., Tadross,
1021 M.R., Patel, R., Zlatic, M., Kim, D.S., Ahrens, M.B., et al. (2015).
1022 Neural circuits. Labeling of active neural circuits in vivo with
1023 designed calcium integrators. *Sci. (N. York, NY)* *347*, 755-760.
1024 <https://doi.org/10.1126/science.1260922>.

1025 22. Edwards, K.A., Hoppa, M.B., and Bosco, G. (2020). The
1026 Photoconvertible Fluorescent Probe, CaMPARI, Labels Active
1027 Neurons in Freely-Moving Intact Adult Fruit Flies. *Front. Neural*
1028 *Circuits* *14*, 22. <https://doi.org/10.3389/fncir.2020.00022>.

1029 23. Moeyaert, B., Holt, G., Madangopal, R., Perez-Alvarez, A.,
1030 Fearey, B.C., Trojanowski, N.F., Ledderose, J., Zolnik, T.A., Das, A.,
1031 Patel, D., et al. (2018). Improved methods for marking active neuron
1032 populations. *Nat. Commun.* *9*, 4440. <https://doi.org/10.1038/s41467-018-06935-2>.

1034 24. Zolnik, T.A., Sha, F., Johenning, F.W., Schreiter, E.R., Looger,
1035 L.L., Larkum, M.E., and Sachdev, R.N.S. (2016). All-optical
1036 functional synaptic connectivity mapping in acute brain slices using
1037 the calcium integrator CaMPARI. *J. Physiol.* *595*, 1465-1477.
1038 <https://doi.org/10.1113/jp273116>.

1039 25. Trojanowski, N.F., Bottorff, J., and Turrigiano, G.G. (2021).
1040 Activity labeling in vivo using CaMPARI2 reveals intrinsic and
1041 synaptic differences between neurons with high and low firing rate

1042 set points. Neuron 109, 663-676.e5.
1043 <https://doi.org/10.1016/j.neuron.2020.11.027>.

1044 26. Das, A., Holden, S., Borovicka, J., Icardi, J., O’Niel, A., Chaklai, A.,
1045 Patel, D., Patel, R., Petrie, S.K., Raber, J., et al. (2023). Large-scale
1046 recording of neuronal activity in freely-moving mice at cellular
1047 resolution. *Nat. Commun.* 14, 6399. <https://doi.org/10.1038/s41467-023-42083-y>.

1049 27. Tian, R., Gachechiladze, M.A., Ludwig, C.H., Laurie, M.T., Hong,
1050 J.Y., Nathaniel, D., Prabhu, A.V., Fernandopulle, M.S., Patel, R.,
1051 Abshari, M., et al. (2019). CRISPR Interference-Based Platform for
1052 Multimodal Genetic Screens in Human iPSC-Derived Neurons.
1053 Neuron 104, 239-255.e12.
1054 <https://doi.org/10.1016/j.neuron.2019.07.014>.

1055 28. Wang, C., Ward, M.E., Chen, R., Liu, K., Tracy, T.E., Chen, X., Xie,
1056 M., Sohn, P.D., Ludwig, C., Meyer-Franke, A., et al. (2017). Scalable
1057 Production of iPSC-Derived Human Neurons to Identify Tau-
1058 Lowering Compounds by High-Content Screening. *Stem Cell Rep.* 9,
1059 1221-1233. <https://doi.org/10.1016/j.stemcr.2017.08.019>.

1060 29. Zhang, Y., Pak, C., Han, Y., Ahlenius, H., Zhang, Z., Chanda, S.,
1061 Marro, S., Patzke, C., Acuna, C., Covy, J., et al. (2013). Rapid Single-
1062 Step Induction of Functional Neurons from Human Pluripotent Stem
1063 Cells. Neuron 78, 785-798.
1064 <https://doi.org/10.1016/j.neuron.2013.05.029>.

1065 30. Shan, X., Zhang, A., Rezzonico, M.G., Tsai, M.-C., Sanchez-
1066 Priego, C., Zhang, Y., Chen, M.B., Choi, M., López, J.M.A., Phu, L., et
1067 al. (2024). Fully defined NGN2 neuron protocol reveals diverse
1068 signatures of neuronal maturation. *Cell Rep. Methods* 4, 100858.
1069 <https://doi.org/10.1016/j.crmeth.2024.100858>.

1070 31. Kosillo, P., Doig, N.M., Ahmed, K.M., Agopyan-Miu, A.H.C.W.,
1071 Wong, C.D., Conyers, L., Threlfell, S., Magill, P.J., and Bateup, H.S.
1072 (2019). Tsc1-mTORC1 signaling controls striatal dopamine release
1073 and cognitive flexibility. *Nat. Commun.* 10, 5426.
1074 <https://doi.org/10.1038/s41467-019-13396-8>.

1075 32. Rao, V.R., and Lowenstein, D.H. (2015). Epilepsy. *Curr. Biol.* 25,
1076 R742-R746. <https://doi.org/10.1016/j.cub.2015.07.072>.

1077 33. Li, W., Xu, H., Xiao, T., Cong, L., Love, M.I., Zhang, F., Irizarry,
1078 R.A., Liu, J.S., Brown, M., and Liu, X.S. (2014). MAGeCK enables
1079 robust identification of essential genes from genome-scale
1080 CRISPR/Cas9 knockout screens. *Genome Biol.* *15*, 554.
1081 <https://doi.org/10.1186/s13059-014-0554-4>.

1082 34. Oliver, K.L., Scheffer, I.E., Bennett, M.F., Grinton, B.E., Bahlo,
1083 M., and Berkovic, S.F. (2023). Genes4Epilepsy: An epilepsy gene
1084 resource. *Epilepsia* *64*, 1368-1375.
1085 <https://doi.org/10.1111/epi.17547>.

1086 35. Mattison, K.A., Tossing, G., Mulroe, F., Simmons, C., Butler,
1087 K.M., Schreiber, A., Alsadah, A., Neilson, D.E., Naess, K., Wedell, A.,
1088 et al. (2022). ATP6V0C variants impair V-ATPase function causing a
1089 neurodevelopmental disorder often associated with epilepsy. *Brain*
1090 *146*, 1357-1372. <https://doi.org/10.1093/brain/awac330>.

1091 36. Bain, J.M., Cho, M.T., Telegrafi, A., Wilson, A., Brooks, S., Botti,
1092 C., Gowans, G., Autullo, L.A., Krishnamurthy, V., Willing, M.C., et al.
1093 (2016). Variants in HNRNPH2 on the X Chromosome Are Associated
1094 with a Neurodevelopmental Disorder in Females. *Am. J. Hum. Genet.*
1095 *99*, 728-734. <https://doi.org/10.1016/j.ajhg.2016.06.028>.

1096 37. Suzuki, H., Yoshida, T., Morisada, N., Uehara, T., Kosaki, K.,
1097 Sato, K., Matsubara, K., Takano-Shimizu, T., and Takenouchi, T.
1098 (2019). De novo NSF mutations cause early infantile epileptic
1099 encephalopathy. *Ann. Clin. Transl. Neurol.* *6*, 2334-2339.
1100 <https://doi.org/10.1002/acn3.50917>.

1101 38. Schubert, J., Siekierska, A., Langlois, M., May, P., Huneau, C.,
1102 Becker, F., Muhle, H., Suls, A., Lemke, J.R., Kovel, C.G.F. de, et al.
1103 (2014). Mutations in STX1B, encoding a presynaptic protein, cause
1104 fever-associated epilepsy syndromes. *Nat. Genet.* *46*, 1327-1332.
1105 <https://doi.org/10.1038/ng.3130>.

1106 39. Fatima, A., Hoeber, J., Schuster, J., Koshimizu, E., Maya-
1107 Gonzalez, C., Keren, B., Mignot, C., Akram, T., Ali, Z., Miyatake, S., et
1108 al. (2021). Monoallelic and bi-allelic variants in NCDN cause
1109 neurodevelopmental delay, intellectual disability, and epilepsy. *Am.*
1110 *J. Hum. Genet.* *108*, 739-748.
1111 <https://doi.org/10.1016/j.ajhg.2021.02.015>.

1112 40. Jaworski, T., Banach-Kasper, E., and Gralec, K. (2019). GSK-3 β at
1113 the Intersection of Neuronal Plasticity and Neurodegeneration.
1114 *Neural Plast.* *2019*, 4209475. <https://doi.org/10.1155/2019/4209475>.

1115 41. Horn, S., Au, M., Basel-Salmon, L., Bayrak-Toydemir, P., Chapin,
1116 A., Cohen, L., Elting, M.W., Graham, J.M., Gonzaga-Jauregui, C.,
1117 Konen, O., et al. (2019). De novo variants in PAK1 lead to intellectual
1118 disability with macrocephaly and seizures. *Brain* *142*, 3351-3359.
1119 <https://doi.org/10.1093/brain/awz264>.

1120 42. Horváth, R., Abicht, A., Holinski-Feder, E., Laner, A., Gempel, K.,
1121 Prokisch, H., Lochmüller, H., Klopstock, T., and Jaksch, M. (2006).
1122 Leigh syndrome caused by mutations in the flavoprotein (Fp) subunit
1123 of succinate dehydrogenase (SDHA). *J. Neurol., Neurosurg.
1124 Psychiatry* *77*, 74. <https://doi.org/10.1136/jnnp.2005.067041>.

1125 43. Salpietro, V., Malintan, N.T., Llano-Rivas, I., Spaeth, C.G.,
1126 Efthymiou, S., Striano, P., Vandrovčova, J., Cutrupi, M.C., Chimenz,
1127 R., David, E., et al. (2019). Mutations in the Neuronal Vesicular
1128 SNARE VAMP2 Affect Synaptic Membrane Fusion and Impair
1129 Human Neurodevelopment. *Am. J. Hum. Genet.* *104*, 721-730.
1130 <https://doi.org/10.1016/j.ajhg.2019.02.016>.

1131 44. Johnstone, D.L., Nguyen, T.T.M., Zambonin, J., Kernohan, K.D.,
1132 St-Denis, A., Baratang, N.V., Hartley, T., Geraghty, M.T., Richer, J.,
1133 Majewski, J., et al. (2020). Early infantile epileptic encephalopathy
1134 due to biallelic pathogenic variants in PIGQ: Report of seven new
1135 subjects and review of the literature. *J. Inherit. Metab. Dis.* *43*, 1321-
1136 1332. <https://doi.org/10.1002/jimd.12278>.

1137 45. Kim, K., Park, I., Kim, J., Kang, M.-G., Choi, W.G., Shin, H., Kim,
1138 J.-S., Rhee, H.-W., and Suh, J.M. (2021). Dynamic tracking and
1139 identification of tissue-specific secretory proteins in the circulation
1140 of live mice. *Nat. Commun.* *12*, 5204.
1141 <https://doi.org/10.1038/s41467-021-25546-y>.

1142 46. Stenmark, H. (2009). Rab GTPases as coordinators of vesicle
1143 traffic. *Nat. Rev. Mol. Cell Biol.* *10*, 513-525.
1144 <https://doi.org/10.1038/nrm2728>.

1145 47. Shin, J., Nile, A., and Oh, J.-W. (2021). Role of adaptin protein
1146 complexes in intracellular trafficking and their impact on diseases.
1147 *Bioengineered* *12*, 8259-8278.
1148 <https://doi.org/10.1080/21655979.2021.1982846>.

1149 48. Liu, Q., Bautista-Gomez, J., Higgins, D.A., Yu, J., and Xiong, Y.
1150 (2021). Dysregulation of the AP2M1 phosphorylation cycle by LRRK2
1151 impairs endocytosis and leads to dopaminergic neurodegeneration.
1152 *Sci. Signal.* **14**. <https://doi.org/10.1126/scisignal.abg3555>.

1153 49. Mouret, R.Z., Greenbaum, J.P., Doll, H.M., Brody, E.M.,
1154 Iacobucci, E.L., Roland, N.C., Simamora, R.C., Ruiz, I., Seymour, R.,
1155 Ludwick, L., et al. (2024). The adaptor protein 2 (AP2) complex
1156 modulates habituation and behavioral selection across multiple
1157 pathways and time windows. *iScience* **27**, 109455.
1158 <https://doi.org/10.1016/j.isci.2024.109455>.

1159 50. Howe, E.N., Burnette, M.D., Justice, M.E., Schnepf, P.M.,
1160 Hedrick, V., Clancy, J.W., Guldner, I.H., Lamere, A.T., Li, J., Aryal,
1161 U.K., et al. (2020). Rab11b-mediated integrin recycling promotes
1162 brain metastatic adaptation and outgrowth. *Nat. Commun.* **11**, 3017.
1163 <https://doi.org/10.1038/s41467-020-16832-2>.

1164 51. Kang, H., Han, A., Zhang, A., Jeong, H., Koh, W., Lee, J.M., Lee,
1165 H., Jo, H.Y., Maria-Solano, M.A., Bhalla, M., et al. (2024). GolpHCat
1166 (TMEM87A), a unique voltage-dependent cation channel in Golgi
1167 apparatus, contributes to Golgi-pH maintenance and hippocampus-
1168 dependent memory. *Nat. Commun.* **15**, 5830.
1169 <https://doi.org/10.1038/s41467-024-49297-8>.

1170 52. Stoetzel, C., Bär, S., Craene, J.-O.D., Scheidecker, S., Etard, C.,
1171 Chicher, J., Reck, J.R., Perrault, I., Geoffroy, V., Chennen, K., et al.
1172 (2016). A mutation in VPS15 (PIK3R4) causes a ciliopathy and affects
1173 IFT20 release from the cis-Golgi. *Nat. Commun.* **7**, 13586.
1174 <https://doi.org/10.1038/ncomms13586>.

1175 53. Koike, S., and Jahn, R. (2019). SNAREs define targeting
1176 specificity of trafficking vesicles by combinatorial interaction with
1177 tethering factors. *Nat. Commun.* **10**, 1608.
1178 <https://doi.org/10.1038/s41467-019-09617-9>.

1179 54. Babst, M., Katzmann, D.J., Estepa-Sabal, E.J., Meerloo, T., and
1180 Emr, S.D. (2002). Escrt-III An endosome-associated
1181 heterooligomeric protein complex required for mvb sorting. *Dev. Cell* **3**, 271-282. [https://doi.org/10.1016/s1534-5807\(02\)00220-4](https://doi.org/10.1016/s1534-5807(02)00220-4).

1183 55. Azmi, I.F., Davies, B.A., Xiao, J., Babst, M., Xu, Z., and Katzmann,
1184 D.J. (2008). ESCRT-III Family Members Stimulate Vps4 ATPase

1185 Activity Directly or via Vta1. *Dev. Cell* *14*, 50–61.
1186 <https://doi.org/10.1016/j.devcel.2007.10.021>.

1187 56. Migliano, S.M., Schultz, S.W., Wenzel, E.M., Takáts, S., Liu, D.,
1188 Mørk, S., Tan, K.W., Rusten, T.E., Raiborg, C., and Stenmark, H.
1189 (2023). Removal of hypersignaling endosomes by simaphagy.
1190 *Autophagy* *20*, 769–791.
1191 <https://doi.org/10.1080/15548627.2023.2267958>.

1192 57. Schluter, C., Lam, K.K.Y., Brumm, J., Wu, B.W., Saunders, M.,
1193 Stevens, T.H., Bryan, J., and Conibear, E. (2008). Global Analysis of
1194 Yeast Endosomal Transport Identifies the Vps55/68 Sorting
1195 Complex. *Mol. Biol. Cell* *19*, 1282–1294.
1196 <https://doi.org/10.1091/mbc.e07-07-0659>.

1197 58. Alsleben, S., and Kölling, R. (2022). Vps68 cooperates with
1198 ESCRT-III in intraluminal vesicle formation. *J. Cell Sci.* *135*.
1199 <https://doi.org/10.1242/jcs.259743>.

1200 59. Longva, K.E., Blystad, F.D., Stang, E., Larsen, A.M., Johannessen,
1201 L.E., and Madshus, I.H. (2002). Ubiquitination and proteasomal
1202 activity is required for transport of the EGF receptor to inner
1203 membranes of multivesicular bodies. *J. Cell Biol.* *156*, 843–854.
1204 <https://doi.org/10.1083/jcb.200106056>.

1205 60. Hurley, J.H., Coyne, A.N., Miączyńska, M., and Stenmark, H.
1206 (2025). The expanding repertoire of ESCRT functions in cell biology
1207 and disease. *Nature* *642*, 877–888. <https://doi.org/10.1038/s41586-025-08950-y>.

1209 61. Neefjes, J., Jongsma, M.M.L., and Berlin, I. (2017). Stop or Go?
1210 Endosome Positioning in the Establishment of Compartment
1211 Architecture, Dynamics, and Function. *Trends Cell Biol.* *27*, 580–594.
1212 <https://doi.org/10.1016/j.tcb.2017.03.002>.

1213 62. Im, Y.J., Wollert, T., Boura, E., and Hurley, J.H. (2009). Structure
1214 and Function of the ESCRT-II-III Interface in Multivesicular Body
1215 Biogenesis. *Dev. Cell* *17*, 234–243.
1216 <https://doi.org/10.1016/j.devcel.2009.07.008>.

1217 63. Stuffers, S., Wegner, C.S., Stenmark, H., and Brech, A. (2009).
1218 Multivesicular Endosome Biogenesis in the Absence of ESCRTs.
1219 *Traffic* *10*, 925–937. <https://doi.org/10.1111/j.1600-0854.2009.00920.x>.

1221 64. Piper, R.C., and Katzmann, D.J. (2007). Biogenesis and Function
1222 of Multivesicular Bodies. *Cell Dev. Biol.* *23*, 519-547.
1223 <https://doi.org/10.1146/annurev.cellbio.23.090506.123319>.

1224 65. Bartheld, C.S.V., and Altick, A.L. (2011). Multivesicular bodies in
1225 neurons: Distribution, protein content, and trafficking functions.
1226 *Prog. Neurobiol.* *93*, 313-340.
1227 <https://doi.org/10.1016/j.pneurobio.2011.01.003>.

1228 66. Cadwell, C.R., Palasantza, A., Jiang, X., Berens, P., Deng, Q.,
1229 Yilmaz, M., Reimer, J., Shen, S., Bethge, M., Tolias, K.F., et al.
1230 (2016). Electrophysiological, transcriptomic and morphologic
1231 profiling of single neurons using Patch-seq. *Nat. Biotechnol.* *34*, 199-
1232 203. <https://doi.org/10.1038/nbt.3445>.

1233 67. Vardar, G., Chang, S., Arancillo, M., Wu, Y.-J., Trimbuch, T., and
1234 Rosenmund, C. (2016). Distinct Functions of Syntaxin-1 in Neuronal
1235 Maintenance, Synaptic Vesicle Docking, and Fusion in Mouse
1236 Neurons. *J. Neurosci.* *36*, 7911-7924.
1237 <https://doi.org/10.1523/jneurosci.1314-16.2016>.

1238 68. Kölling, R. (2024). Interaction between ESCRT-III proteins and
1239 the yeast SERINC homolog Tms1. *GENETICS* *228*, iyae132.
1240 <https://doi.org/10.1093/genetics/iyae132>.

1241 69. Picon, C., Aleksynas, R., Wojewska, M., Virgiliis, F. de, Merkler,
1242 D., and Reynolds, R. (2025). Dysregulation of the endosomal sorting
1243 complex III is linked to neurodegeneration in progressive multiple
1244 sclerosis. *Brain Pathol.* *36*, e70034.
1245 <https://doi.org/10.1111/bpa.70034>.

1246 70. Coulter, M.E., Dorobantu, C.M., Lodewijk, G.A., Delalande, F.,
1247 Cianferani, S., Ganesh, V.S., Smith, R.S., Lim, E.T., Xu, C.S., Pang,
1248 S., et al. (2018). The ESCRT-III Protein CHMP1A Mediates Secretion
1249 of Sonic Hedgehog on a Distinctive Subtype of Extracellular
1250 Vesicles. *Cell Rep.* *24*, 973-986.e8.
1251 <https://doi.org/10.1016/j.celrep.2018.06.100>.

1252 71. Lee, J.-A., Beigneux, A., Ahmad, S.T., Young, S.G., and Gao, F.-B.
1253 (2007). ESCRT-III Dysfunction Causes Autophagosome
1254 Accumulation and Neurodegeneration. *Curr. Biol.* *17*, 1561-1567.
1255 <https://doi.org/10.1016/j.cub.2007.07.029>.

1256 72. Boggess, S.C., Gandhi, V., Tsai, M.-C., Marzette, E., Teyssier, N.,
1257 Chou, J.Y.-Y., Hu, X., Cramer, A., Yadanar, L., Shroff, K., et al. (2025).
1258 A Massively Parallel CRISPR-Based Screening Platform for Modifiers
1259 of Neuronal Activity. *bioRxiv*, 2024.02.28.582546.
1260 <https://doi.org/10.1101/2024.02.28.582546>.

1261 73. Beaudoin, G.M.J., Lee, S.-H., Singh, D., Yuan, Y., Ng, Y.-G.,
1262 Reichardt, L.F., and Arikath, J. (2012). Culturing pyramidal neurons
1263 from the early postnatal mouse hippocampus and cortex. *Nat. Protoc.* 7, 1741–1754. <https://doi.org/10.1038/nprot.2012.099>.

1265 74. Labun, K., Montague, T.G., Krause, M., Cleuren, Y.N.T., Tjeldnes,
1266 H., and Valen, E. (2019). CHOPCHOP v3: expanding the CRISPR web
1267 toolbox beyond genome editing. *Nucleic Acids Res.* 47, W171–W174.
1268 <https://doi.org/10.1093/nar/gkz365>.

1269 75. Zeng, Q., Li, Y., Wu, Y., Wu, J., Xu, K., Chen, Y., Rao, Y., Li, N.,
1270 Luo, Y., Jiang, C., et al. (2025). Neuropeptide Y neurons mediate
1271 opioid-induced itch by disinhibiting GRP-GRPR microcircuits in the
1272 spinal cord. *Nat. Commun.* 16, 7074.
1273 <https://doi.org/10.1038/s41467-025-62382-w>.

1274 76. Shan, L., Xu, K., Ji, L., Zeng, Q., Liu, Y., Wu, Y., Chen, Y., Li, Y.,
1275 Hu, Q., Wu, J., et al. (2024). Injured sensory neurons-derived
1276 galectin-3 contributes to neuropathic pain via programming
1277 microglia in the spinal dorsal horn. *Brain, Behav., Immun.* 117, 80–
1278 99. <https://doi.org/10.1016/j.bbi.2024.01.002>.

1279 77. Petkovic, M., Oses-Prieto, J., Burlingame, A., Jan, L.Y., and Jan,
1280 Y.N. (2020). TMEM16K is an interorganelle regulator of endosomal
1281 sorting. *Nat. Commun.* 11, 3298. <https://doi.org/10.1038/s41467-020-17016-8>.

1283 78. Hale, W.D., Südhof, T.C., and Huganir, R.L. (2023). Engineered
1284 adhesion molecules drive synapse organization. *Proc. Natl. Acad.
1285 Sci.* 120, e2215905120. <https://doi.org/10.1073/pnas.2215905120>.

1286 79. Kraeuter, A.-K., Guest, P.C., and Sarnyai, Z. (2018). The Open
1287 Field Test for Measuring Locomotor Activity and Anxiety-Like
1288 Behavior. *Methods Mol. Biol.* (Clifton, NJ) 1916, 99–103.
1289 https://doi.org/10.1007/978-1-4939-8994-2_9.

1290 80. Wang, G., Peng, S., Mendez, M.R., Keramidas, A., Castellano, D.,
1291 Wu, K., Han, W., Tian, Q., Dong, L., Li, Y., et al. (2024). The

93

1292 TMEM132B-GABAA receptor complex controls alcohol actions in the
1293 brain. *Cell* 187, 6649-6668.e35.
1294 <https://doi.org/10.1016/j.cell.2024.09.006>.

1295 81. Hallgren, J., Tsirigos, K.D., Pedersen, M.D., Armenteros, J.J.A.,
1296 Marcatili, P., Nielsen, H., Krogh, A., and Winther, O. (2022).
1297 DeepTMHMM predicts alpha and beta transmembrane proteins
1298 using deep neural networks.
1299 <https://doi.org/10.1101/2022.04.08.487609>.

1300

1301

94

95

1302 **ACKNOWLEDGEMENTS**

1303 We thank the assistance of SUSTech Core Research Facilities on flow
1304 cytometry. We also would like to acknowledge the SZBL Bio-Imaging
1305 core for assistance with the SEM sample preparation and imaging.

1306

1307 **Funding**

1308 National Key Research and Development Program of China
1309 2024YFA0919800 (RT)

1310 Shenzhen Medical Research Fund A2303039 (RT)

1311 Shenzhen Medical Research Fund C2301006 (ZW)

1312 Guangdong Basic and Applied Basic Research Foundation
1313 2023B1515020075 (RT)

1314 Key Area Research and Development Program of Guangdong
1315 Province 2023B0303010002 (ZW)

1316 Shenzhen Fundamental Research Program
1317 RCYX20221008092845052 (RT)

1318 Lingang Laboratory Grant LGL-3142-ADB24020 (XJ)

1319

1320 **Author contributions**

1321 Conceptualization: RT, XJ

1322 Investigation: JW, ML, YC, JC, XZ

1323 Supervision: ZW, XJ, RT

1324 Writing - original draft: JW, ML, RT

1325 Writing - review & editing: All authors.

1326

1327 **Competing interests**

1328 All other authors declare they have no competing interests.

1329

1330 **Data and materials availability**

96

97

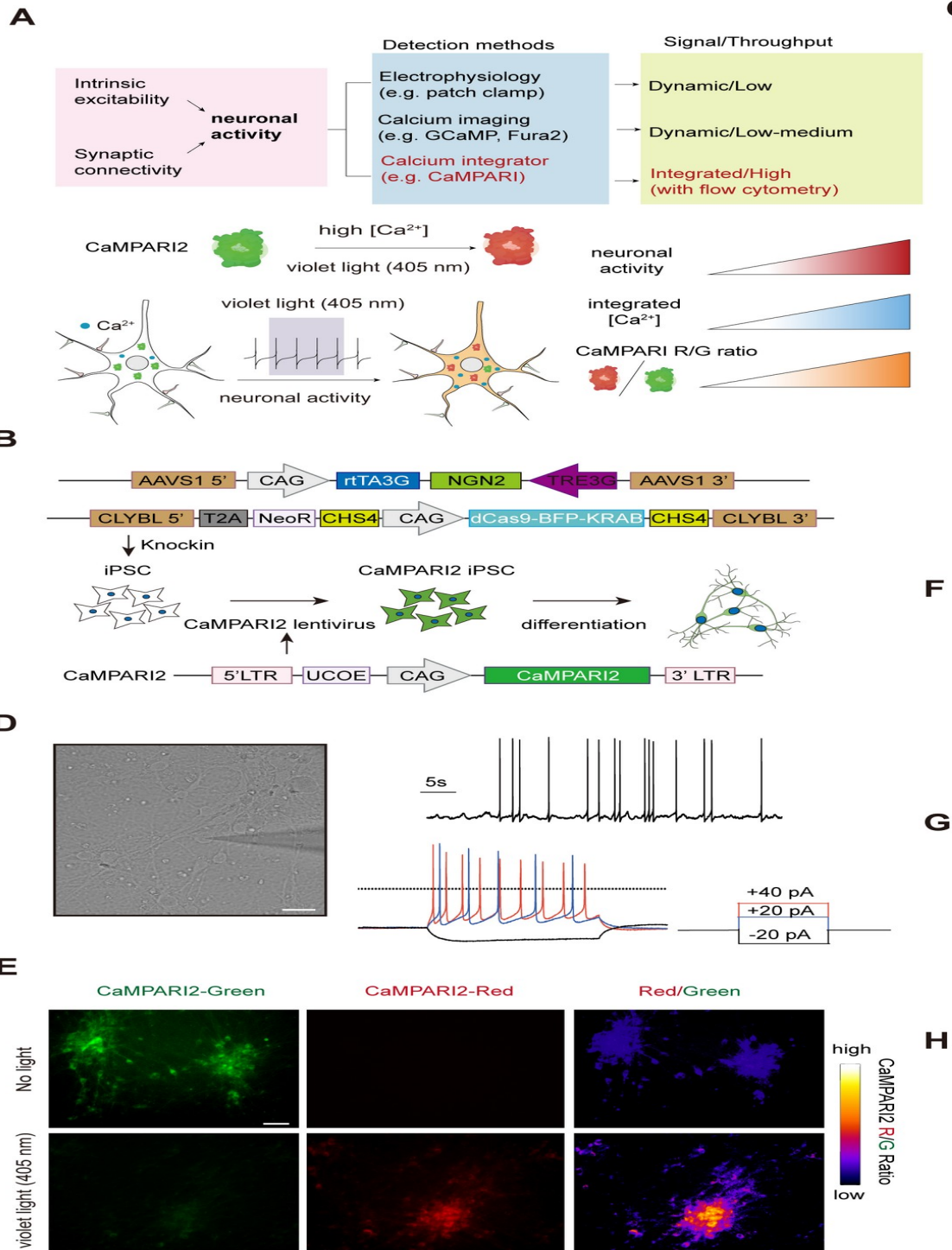
1331 All data are available in the main text or the supplementary
1332 materials.

1333

1334

98

1335 **FIGURES AND FIGURE LEGENDS**



1336

1337 **Figure 1. Establishment of a CaMPARI2-based high-**
 1338 **throughput platform for quantifying neuronal activity in**
 1339 **human iNeurons**

1340 (A) Schematic comparison of major approaches for measuring

101

1341 neuronal activity. Electrophysiology provides gold-standard but
1342 low-throughput measurements; calcium and voltage imaging
1343 capture transient activity in low- to medium-throughput arrayed
1344 formats; CaMPARI2 converts cumulative Ca^{2+} activity during a
1345 defined illumination window into a stable red/green fluorescence
1346 ratio that can be quantified at single-cell resolution by flow
1347 cytometry, enabling pooled genetic screening.

1348 (B) Strategy for integrating CaMPARI2 into the CRISPRi iNeuron
1349 platform. Human iPSCs carry a doxycycline-inducible NGN2 cassette
1350 at the AAVS1 locus and a dCas9-BFP-KRAB cassette at the CLYBL
1351 locus. CaMPARI2 is introduced by lentiviral transduction under a
1352 CAG promoter. Upon doxycycline induction, iPSCs rapidly
1353 differentiate into glutamatergic iNeurons expressing CaMPARI2 and
1354 CRISPRi machinery.

1355 (C) Transcriptomic maturation of iNeurons. Heatmap showing
1356 expression dynamics of representative neuronal activity-related
1357 genes (including ion channels, glutamate receptors, vesicle release
1358 machinery, and synaptic components) across days 14, 21, 28, and 35
1359 of differentiation. Expression of activity-associated genes increases
1360 after day 14 and plateaus around days 21–28.

1361 (D) Functional maturation of iNeurons by electrophysiology. Left,
1362 DIC image of day 28 iNeurons (scale bar, 10 μm). Right,
1363 representative traces of spontaneous (top) and evoked (bottom)
1364 action potential in day 28 iNeurons.

1365 (E) Representative confocal images of CaMPARI2-iNeurons before
1366 and after 5 min of 405 nm violet light illumination. Panels show green
1367 fluorescence, red fluorescence, and green-to-red ratio. Scale bar: 10
1368 μm .

1369 (F) Quantification of CaMPARI2 photoconversion by flow cytometry

102

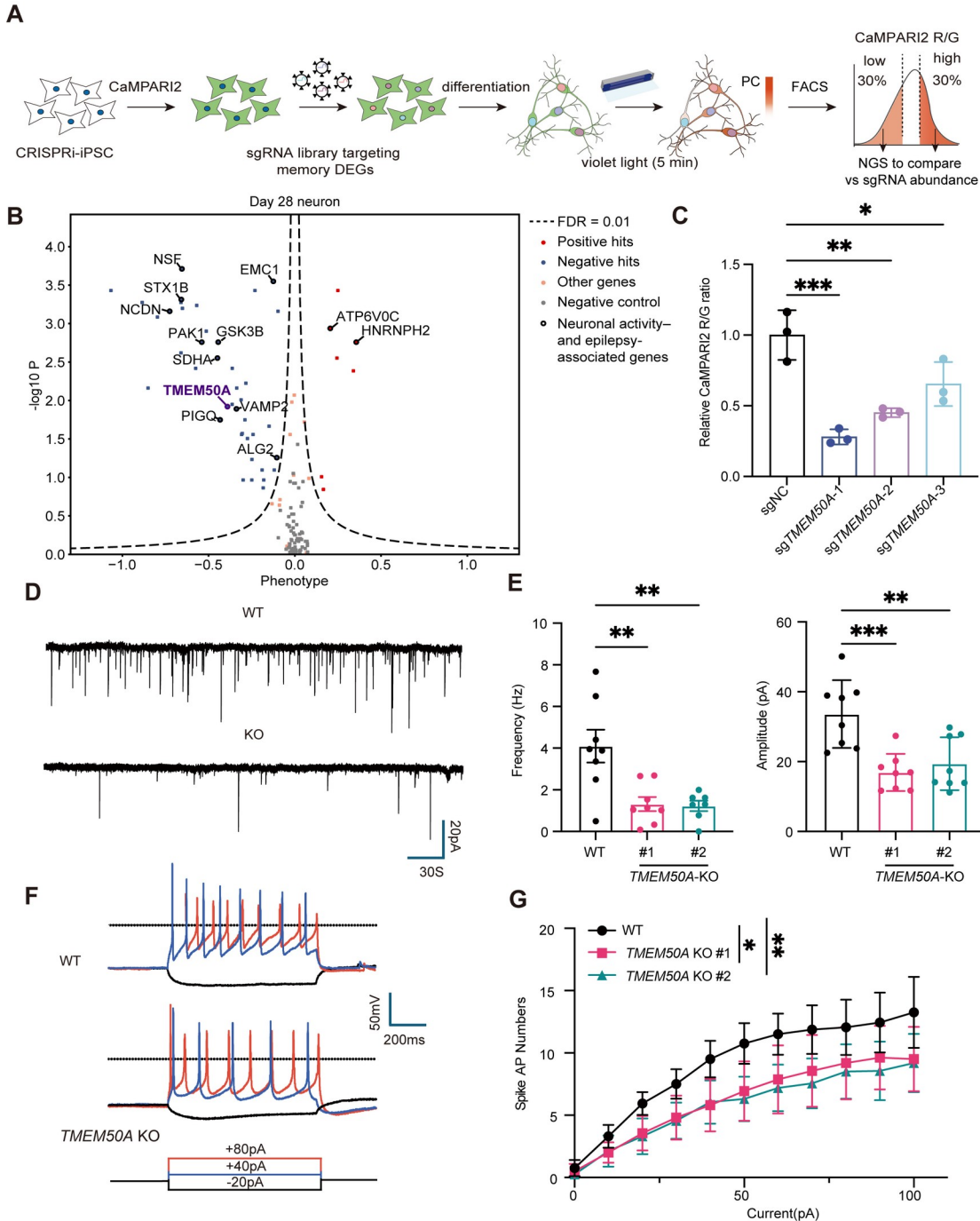
103

1370 as a function of illumination time. CaMPARI2 red-to-green (R/G)
1371 fluorescence ratio increases with longer illumination duration (0–10
1372 min). Data are presented as mean \pm SD. n = 3 biological replicates
1373 per condition.

1374 (G) Dose-dependent increase in CaMPARI2 R/G ratio upon glutamate
1375 stimulation. iNeurons were treated with increasing concentrations
1376 of glutamate (0–100 μ M) for 5 min during violet light illumination.
1377 Data are presented as mean \pm SD. n = 3 biological replicates per
1378 condition.

1379 (H) CaMPARI2 detects genetically driven changes in neuronal
1380 activity. Quantification of CaMPARI2 R/G ratio in control iNeurons
1381 (NTC) versus iNeurons with CRISPRi-mediated knockdown of *TSC1*
1382 or *STXBP1* under 1 min (left) or 5 min (right) illumination. Data are
1383 presented as mean \pm SD. n = 3 biological replicates per condition.

104



1385 **Figure 2. A CaMPARI2-based CRISPRi screen identifies**
1386 **TMEM50A as an essential regulator of neuronal activity**
1387 (A) Schematic of the CaMPARI2-CRISPRi screening workflow.
1388 CRISPRi-iPSCs expressing CaMPARI2 were transduced with an
1389 sgRNA library targeting memory-associated DEGs. Following
1390 differentiation into iNeurons, cells were subjected to 5 min of violet

107

1391 light photoconversion (PC), dissociated, and sorted by FACS based
1392 on CaMPARI2 red-to-green (R/G) ratio. The top 30% (high activity)
1393 and bottom 30% (low activity) populations were collected, and
1394 sgRNA representation was quantified by next-generation sequencing
1395 (NGS) to identify hits.

1396 (B) Volcano plot showing the CaMPARI2 screen results. The x axis
1397 indicates the activity phenotype score (negative values, decreased
1398 CaMPARI2 signal upon knockdown; positive values, increased
1399 signal), and the y axis indicates $-\log_{10} P$ from MAGeCK-iNC analysis.
1400 Dashed line marks FDR = 0.01. Selected known neuronal activity-
1401 and epilepsy-associated genes are labeled. *TMEM50A*, a gene of
1402 previously unknown function, is highlighted in purple.

1403 (C) Validation of *TMEM50A* as a negative hit from the screen.
1404 Relative CaMPARI2 R/G ratio in iNeurons transduced with non-
1405 targeting control sgRNA (sgNTC) or three independent sgRNAs
1406 targeting *TMEM50A* (sgTMEM50A-1, -2, -3). Data are normalized to
1407 sgNTC and presented as mean \pm SD (n = 3 biological replicates). *p
1408 < 0.05, **p < 0.01, ***p < 0.001, one-way ANOVA.

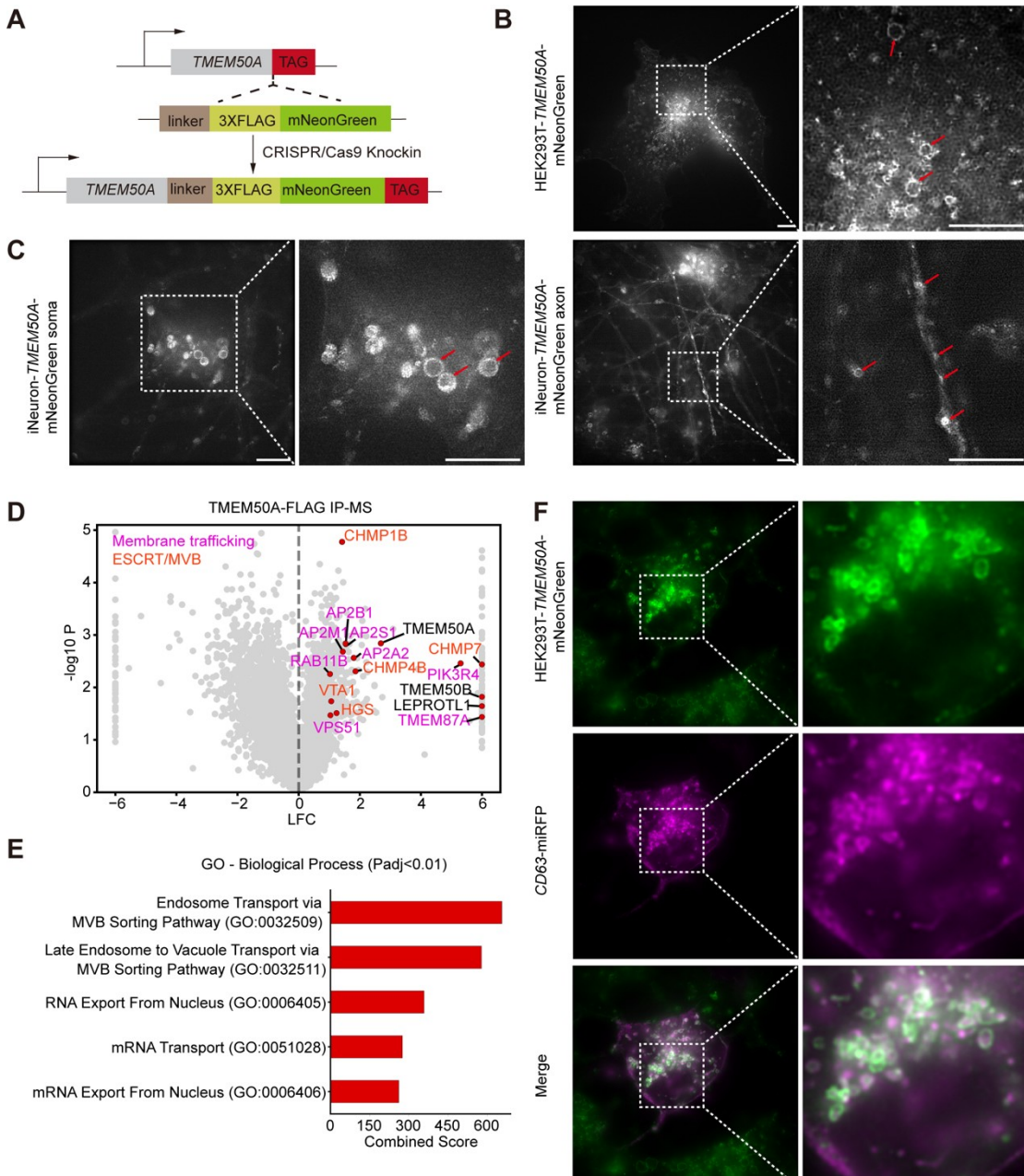
1409 (D-E) *TMEM50A* loss impairs excitatory synaptic transmission. (D)
1410 Representative voltage-clamp traces of sEPSCs in WT and
1411 *TMEM50A* KO iNeurons. Scale bars: 20 pA, 30 s. (E) Quantification
1412 of sEPSC frequency (left) and amplitude (right) in WT and two
1413 independent *TMEM50A* KO lines (#1, #2). Each dot represents one
1414 cell. Data are presented as mean \pm SEM (n = 8 neurons). *p < 0.05,
1415 **p < 0.01, ***p < 0.001, one-way ANOVA.

1416 (F-G) *TMEM50A* loss reduces intrinsic excitability. (F)
1417 Representative current-clamp recordings showing action potential
1418 firing in response to current injections (-20, +40, +80 pA; 300 ms)
1419 in WT and *TMEM50A* KO iNeurons. Scale bars: 50 mV, 200 ms. (G)

108

109

1420 Input-output curves showing the number of action potentials evoked
1421 as a function of injected current for WT and *TMEM50A* KO (#1, #2)
1422 iNeurons. Data are presented as mean \pm SEM (n = 16 neurons). *p <
1423 0.05, **p < 0.01, Two-way ANOVA Bonferroni's multiple
1424 comparisons.



1425

1426 **Figure 3. TMEM50A localizes to multivesicular bodies**

1427 (A) Schematic of CRISPR/Cas9-mediated endogenous tagging
1428 strategy. A C-terminal 3xFLAG-mNeonGreen cassette was inserted

110

111

1429 in-frame at the TMEM50A locus to generate TMEM50A-3xFLAG-
1430 mNeonGreen knock-in (KI) cells.

1431 (B-C) Super-resolution imaging of endogenously tagged TMEM50A-
1432 mNeonGreen. TMEM50A shows a punctate, vesicular distribution in
1433 HEK293T KI cells and in iNeurons, with TMEM50A-positive vesicles
1434 present in both soma and neurites. Magnified views highlight
1435 representative TMEM50A-positive vesicles (red arrows). Scale bars,
1436 5 μ m.

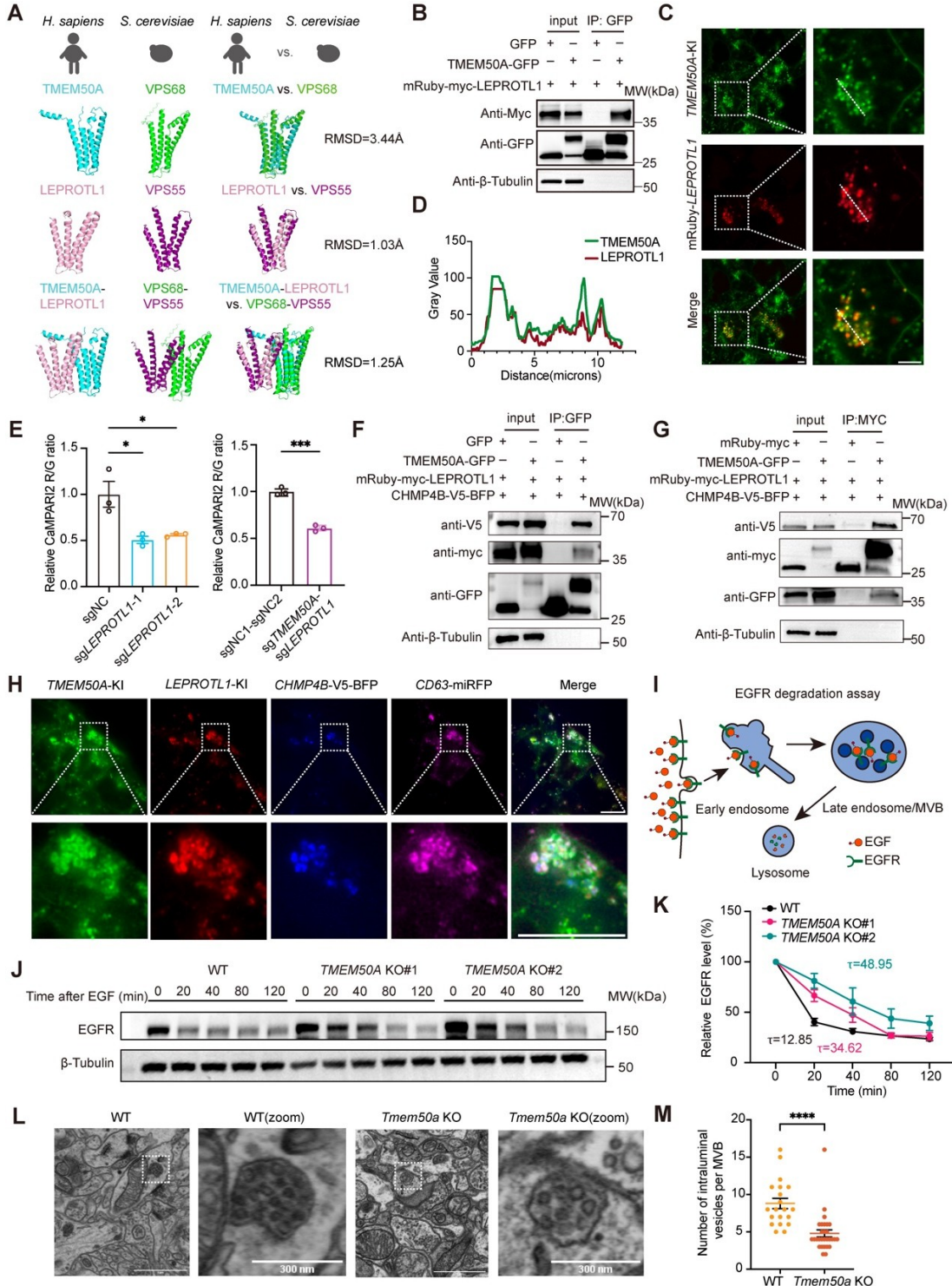
1437 (D) Volcano plot of proteins identified by TMEM50A-FLAG
1438 immunoprecipitation-mass spectrometry (IP-MS) in iNeurons. The x
1439 axis shows \log_2 fold change (LFC) relative to IgG control and the y
1440 axis shows $-\log_{10}$ P. TMEM50A and selected enriched interactors
1441 involved in membrane trafficking (magenta) and ESCRT/MVB
1442 function (orange) are labeled.

1443 (E) Gene Ontology (GO) enrichment analysis of TMEM50A
1444 interactors ($P_{adj} < 0.01$).

1445 (F) Co-localization of TMEM50A with the MVB marker CD63.
1446 Representative confocal images of HEK293T TMEM50A-
1447 mNeonGreen KI cells (green) co-expressing CD63-miRFP
1448 (magenta). Scale bars, 5 μ m.

1449

112



1451 **Figure 4. TMEM50A forms a complex with LEPROT1 and**
 1452 **ESCRT-III to support MVB function**
 1453 (A) Structural conservation of the TMEM50A-LEPROTL1 complex.
 1454 AlphaFold3-based models of human TMEM50A and LEPROT1 and

115

1455 their yeast homologs Vps68 and Vps55, shown individually and as
1456 complexes.

1457 (B) Co-immunoprecipitation (co-IP) showing interaction between
1458 TMEM50A and LEPROT1. HEK293T cells expressing TMEM50A-
1459 GFP and mRuby-myc-LEPROTL1 were subjected to GFP
1460 immunoprecipitation followed by immunoblotting with anti-Myc and
1461 anti-GFP; β -tubulin, loading control.

1462 (C-D) Co-localization of TMEM50A and LEPROT1 in cells. (C)
1463 Representative fluorescence images of TMEM50A knock-in (KI) cells
1464 expressing mRuby-myc-LEPROTL1; Scale bars, 5 μ m. (D) Line-scan
1465 intensity profiles across the indicated region show correlated
1466 TMEM50A and LEPROT1 signals.

1467 (E) Functional epistasis analysis. CaMPARI2 R/G ratio in iNeurons
1468 with CRISPRi-mediated knockdown of *LEPROTL1* individually (left)
1469 or in combination with *TMEM50A* (right). Double knockdown does
1470 not enhance the phenotype relative to single knockdowns, indicating
1471 that TMEM50A and LEPROT1 function in the same pathway.
1472 Relative R/G ratios normalized to control sgRNA are shown as mean
1473 \pm SD (n = 3 biological replicates). *p < 0.05, **p < 0.01, ***p < 0.001,
1474 One-way ANOVA.

1475 (F-G) Co-IP demonstrating interactions among TMEM50A,
1476 LEPROT1, and the ESCRT-III component CHMP4B. (F) Anti-GFP IP
1477 from cells co-expressing mRuby-myc, TMEM50A-GFP, mRuby-myc-
1478 LEPROT1, and CHMP4B-V5-BFP. (G) Anti-Myc IP from cells co-
1479 expressing the same constructs.

1480 (H) Co-localization of TMEM50A, LEPROT1, CHMP4B, and CD63 at
1481 MVBs. Representative confocal images of cells co-expressing
1482 TMEM50A-mNeonGreen (green), LEPROT1-mRuby (red),
1483 CHMP4B-V5-BFP (blue), and CD63-mRFP (magenta). Scale bars, 5

116

117

1484 μ m.

1485 (I) Schematic of the EGFR degradation assay.

1486 (J-K) TMEM50A is required for efficient EGFR degradation. (J) Time-
1487 course Western blots of EGFR levels following EGF stimulation in WT
1488 and two independent *TMEM50A* knockout (KO#1, KO#2) HEK293T
1489 cell lines; β -Tubulin serves as a loading control. (K) Quantification of
1490 relative EGFR levels (normalized to time 0) plotted over time KO
1491 cells show a slower EGFR degradation rate compared to WT cells.
1492 The decay rates (τ) for each condition are indicated on the graph.

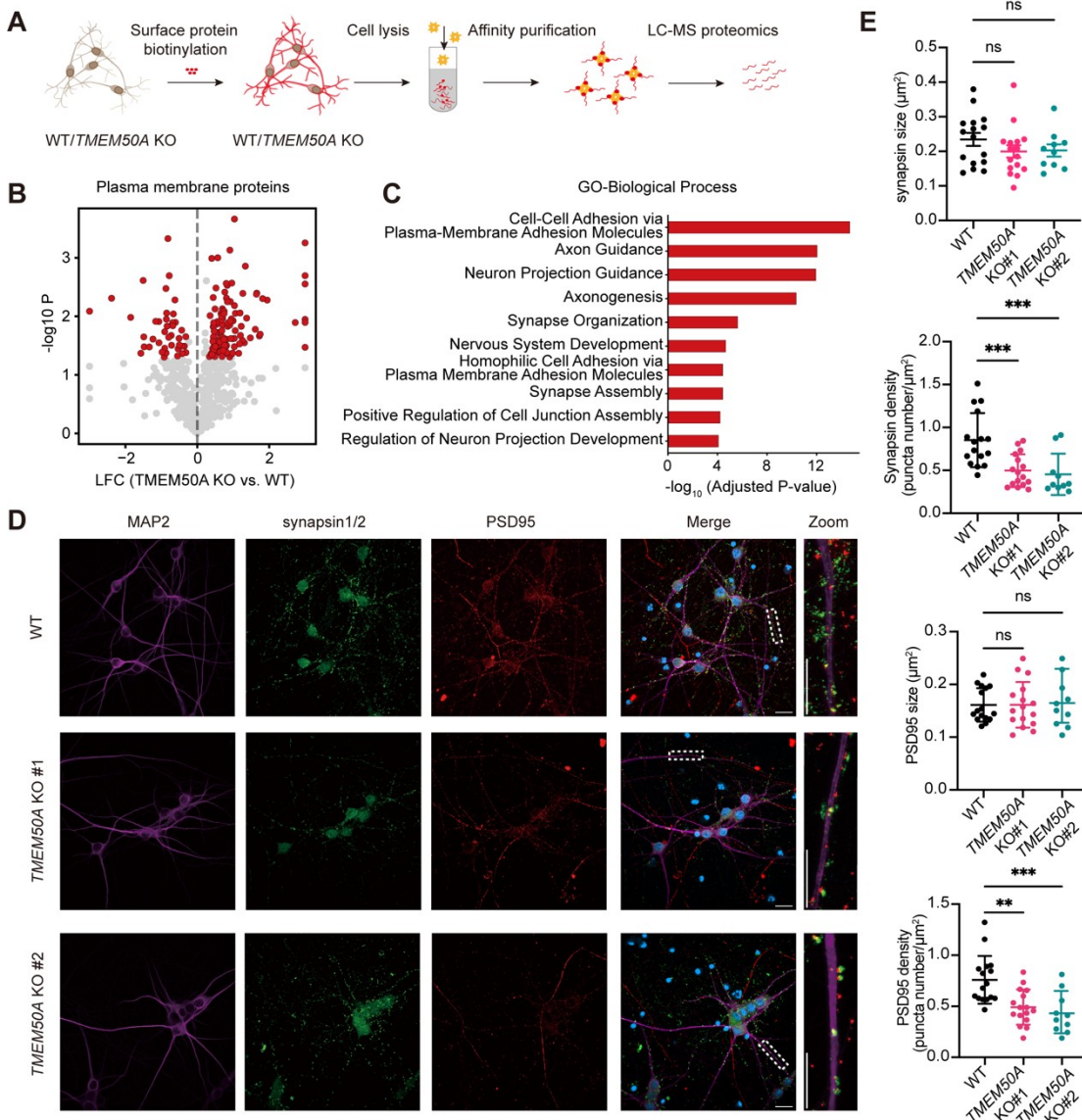
1493 Data are presented as mean \pm SEM (n = 3 biological replicates).

1494 (L-M) *Tmem50a* loss reduces intraluminal vesicle (ILV) formation in
1495 MVBs *in vivo*. (L) Representative scanning electron microscopy
1496 (SEM) images of MVBs from the anterior cingulate cortex (ACC) of
1497 WT and *Tmem50a*-KO mice. Scale bars, as indicated. (M)
1498 Quantification of ILV number per MVB. Each dot represents one
1499 MVB; Data are presented as mean \pm SEM (WT: n = 20; *Tmem50a*-
1500 KO: n = 29). ***p < 0.0001, one-way ANOVA.

1501

1502

118



1503

1504 **Figure 5. *TMEM50A* loss remodels the neuronal surface**

1505 **proteome and reduces synapse density in human iNeurons**

1506 (A) Schematic of the surface proteomics workflow. WT and

1507 *TMEM50A* KO iNeurons were subjected to cell-surface protein

1508 biotinylation, followed by cell lysis, affinity purification of

1509 biotinylated proteins, and LC-MS/MS analysis.

1510 (B) Volcano plot of plasma membrane proteins comparing *TMEM50A*

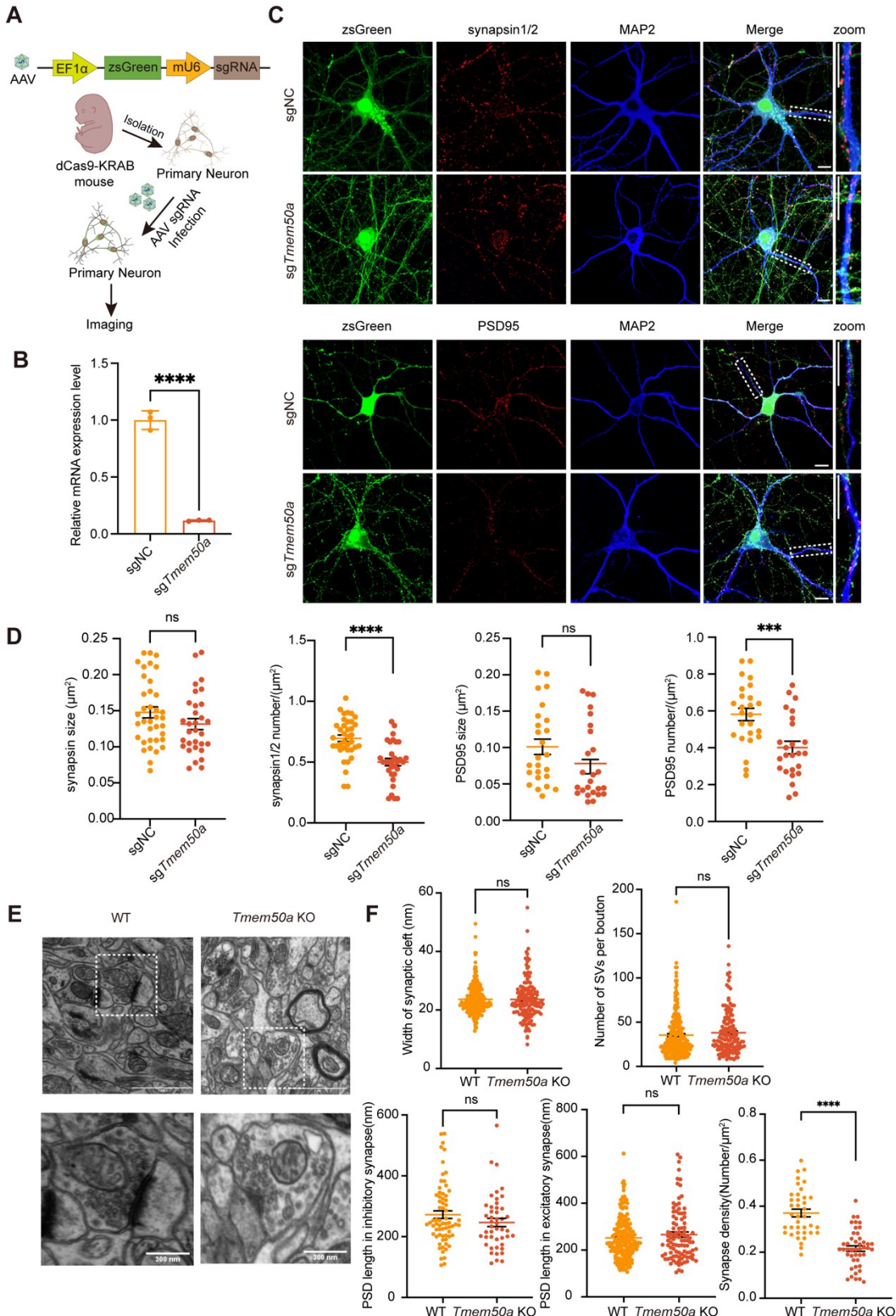
1511 KO versus WT iNeurons. Significantly altered surface proteins are

1512 highlighted in red.

121

1513 (C) Gene Ontology (GO) enrichment analysis (Biological Process) of
1514 significantly changed surface proteins in *TMEM50A* KO neurons. Top
1515 10 significantly enriched terms are shown.
1516 (D) Representative confocal images of WT and *TMEM50A* KO
1517 iNeuron lines stained for MAP2 (dendrites, purple), synapsin1/2
1518 (presynaptic marker, green), and PSD95 (postsynaptic marker, red).
1519 Merged and zoomed views (right) show synaptic puncta along MAP2
1520 dendrites. Scale bars, 10 μ m.
1521 (E) Quantification of synaptic puncta. Top: synapsin1/2 puncta size
1522 per neuron; second: synapsin1/2 puncta density per μ m dendrite
1523 length; third: PSD95 puncta size; bottom: PSD95 puncta density.
1524 Data are presented as mean \pm SEM (WT: n = 16; *TMEM50A* KO #1:
1525 n= 16; *TMEM50A* KO #2: n=10). ns, not significant, **p < 0.01, ***p
1526 < 0.001, one-way ANOVA.
1527

122



1529 **Figure 6. *Tmem50a* loss decreases synapse density in primary**
 1530 **neurons and *in vivo***

125

1531 (A) Schematic of CRISPRi-mediated knockdown of *Tmem50a* in
1532 primary cortical neurons. Primary neurons from dCas9-KRAB mice
1533 were infected with AAV expressing either a non-targeting control
1534 sgRNA (sgNC) or a *Tmem50a*-targeting sgRNA together with
1535 zsGreen for labeling.

1536 (B) qRT-PCR validation of *Tmem50a* knockdown efficiency in primary
1537 neurons transduced with sg *Tmem50a* compared with sgNC. Data are
1538 presented as mean \pm SD (n = 3 biological replicates). **** P <
1539 0.0001, unpaired t test.

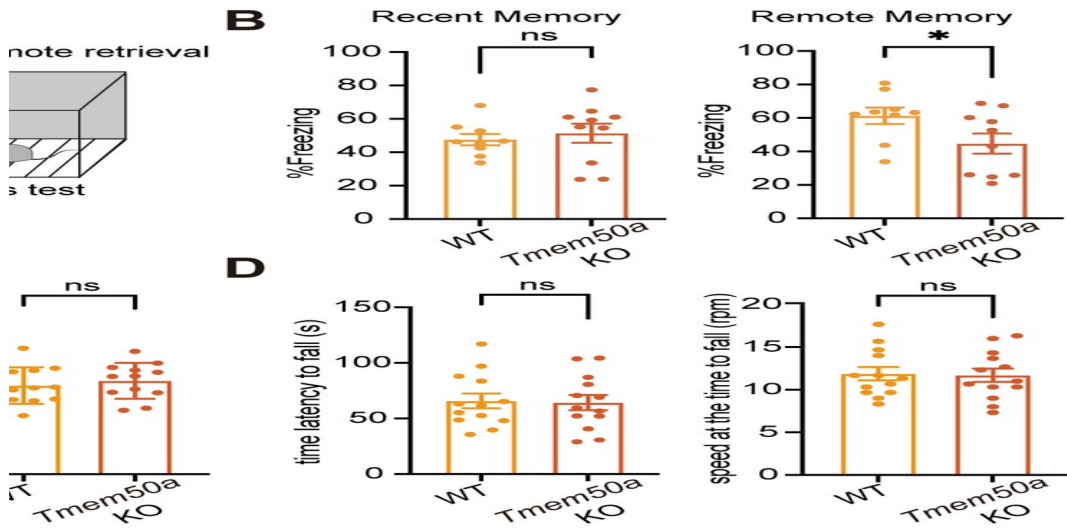
1540 (C) Representative immunofluorescence images of sgNC and
1541 sg *Tmem50a* primary neurons stained for synapsin1/2 (up, red) or
1542 PSD95 (bottom, red) together with MAP2 (blue), with zoomed-in
1543 views showing synaptic puncta. zsGreen, infection marker. Scale
1544 bars: 10 μ m.

1545 (D) Quantification of Synapsin1/2 and PSD95 puncta density and size
1546 in sgNC and sg *Tmem50a* neurons. Data are presented as mean \pm
1547 SEM (synapsin1/2 sgNC: n = 37, sg *Tmem50a*: n = 31; PSD95 sgNC:
1548 n = 25, sg *Tmem50a*: n = 25). ns, not significant, ***p < 0.001, ****p
1549 < 0.0001, unpaired t test.

1550 (E) Representative electron microscopy images of the ultrastructural
1551 of synapse in the ACC region of WT and *Tmem50a*-KO mouse brain
1552 tissue. Scale bars, as indicated.

1553 (F) Quantification of synaptic cleft width (WT n = 237, KO n = 146),
1554 synaptic vesicle (SV) number per bouton (WT n = 233, KO n = 151),
1555 PSD length at inhibitory (WT n = 64, KO n = 48) and excitatory
1556 synapses (WT n = 175, KO n = 100), and synapse density (WT n = 38,
1557 KO n = 45) in the ACC region of WT and *Tmem50a*-KO mouse brain
1558 tissue. Data are presented as mean \pm SEM. ns, not significant, ****p
1559 < 0.0001, unpaired t-test.

126



1560

1561 **Figure 7. *Tmem50a* loss impairs remote memory and alters**
1562 **anxiety-like behavior without affecting motor coordination**

1563 (A) Schematic of the contextual fear conditioning paradigm.

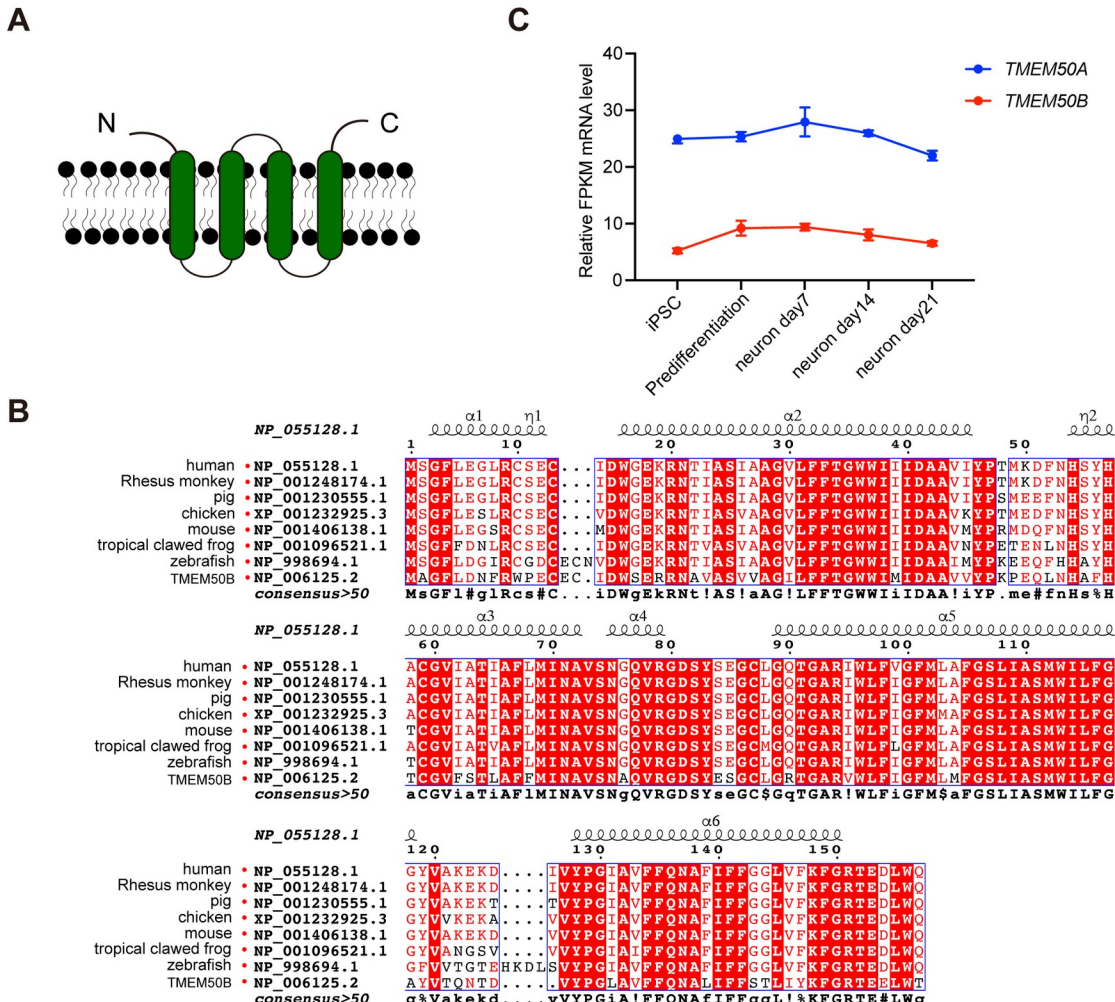
1564 (B) Freezing behavior during recent (Day 5) and remote (Day 21)
1565 memory retrieval. *Tmem50a*-KO mice show normal recent memory
1566 but significantly reduced freezing during remote memory retrieval
1567 compared with WT controls. Data are presented as mean \pm SEM (WT
1568 mice: n = 9, KO mice: n = 10). ns, not significant, *p < 0.05, unpaired
1569 t test.

1570 (C) Open field test. Left: representative locomotor traces of WT and
1571 *Tmem50a*-KO mice (central zone outlined in green). Right:
1572 quantification of time spent in the central zone and total distance
1573 traveled. *Tmem50a*-KO mice spend more time in the center (reduced
1574 anxiety-like behavior) with no change in total distance. Data are
1575 presented as mean \pm SEM (n = 12). ns, not significant, *p < 0.05,
1576 unpaired t test.

1577 (D) Rotarod test. Latency to fall and speed at the time of fall are
1578 shown for WT and *Tmem50a*-KO mice. No significant differences
1579 were observed, indicating normal motor coordination and balance.

1580 Data are presented as mean \pm SEM (n=13). ns, not significant,
1581 unpaired t test.

1582



1583

1584 **Figure S1. TMEM50A is a conserved four-pass transmembrane**

1585 protein and is the predominant paralog in iNeurons

1586 (A) Predicted membrane topology model of TMEM50A based on

1587 TMHMM analysis⁸¹ showing four transmembrane helices (green)

1588 with both N- and C-termini facing the cytosol.

1589 (B) Protein sequence alignment of TMEM50A. The alignment was

1590 created with ESPript 3.0 alignment editor. The protein sources and

1591 their NCBI accession numbers are indicated. Conserved residues are

1592 highlighted in red, and predicted α -helices (α_1 - α_6) are indicated

131

1593 above the alignment. *TMEM50A* is highly conserved across
1594 vertebrates.

1595 (C) Expression profiles of *TMEM50A* (blue) and *TMEM50B* (red)
1596 during iNeuron differentiation, quantified from RNA-seq as relative
1597 FPKM. *TMEM50A* is expressed at higher levels than *TMEM50B* at all
1598 stages. Data are presented as mean \pm SD (n = 3 biological
1599 replicates).

132

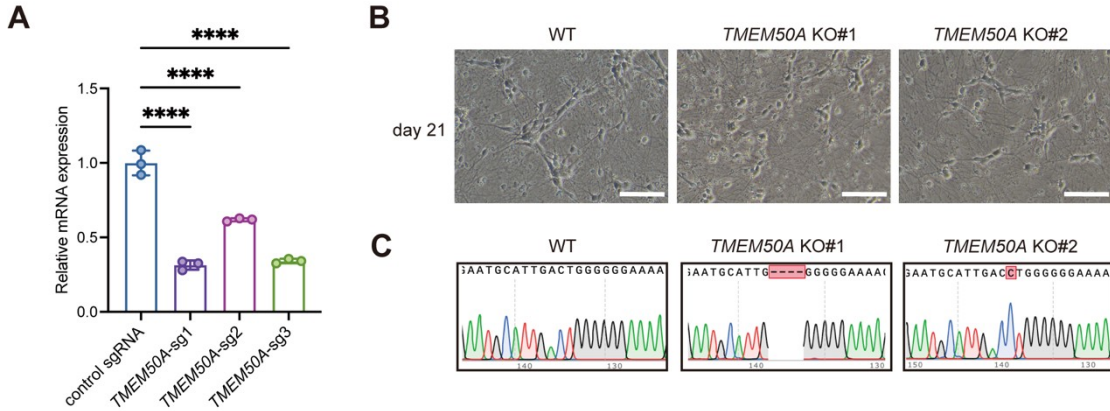


Figure S2. Validation of *TMEM50A* knockdown and KO in iNeurons

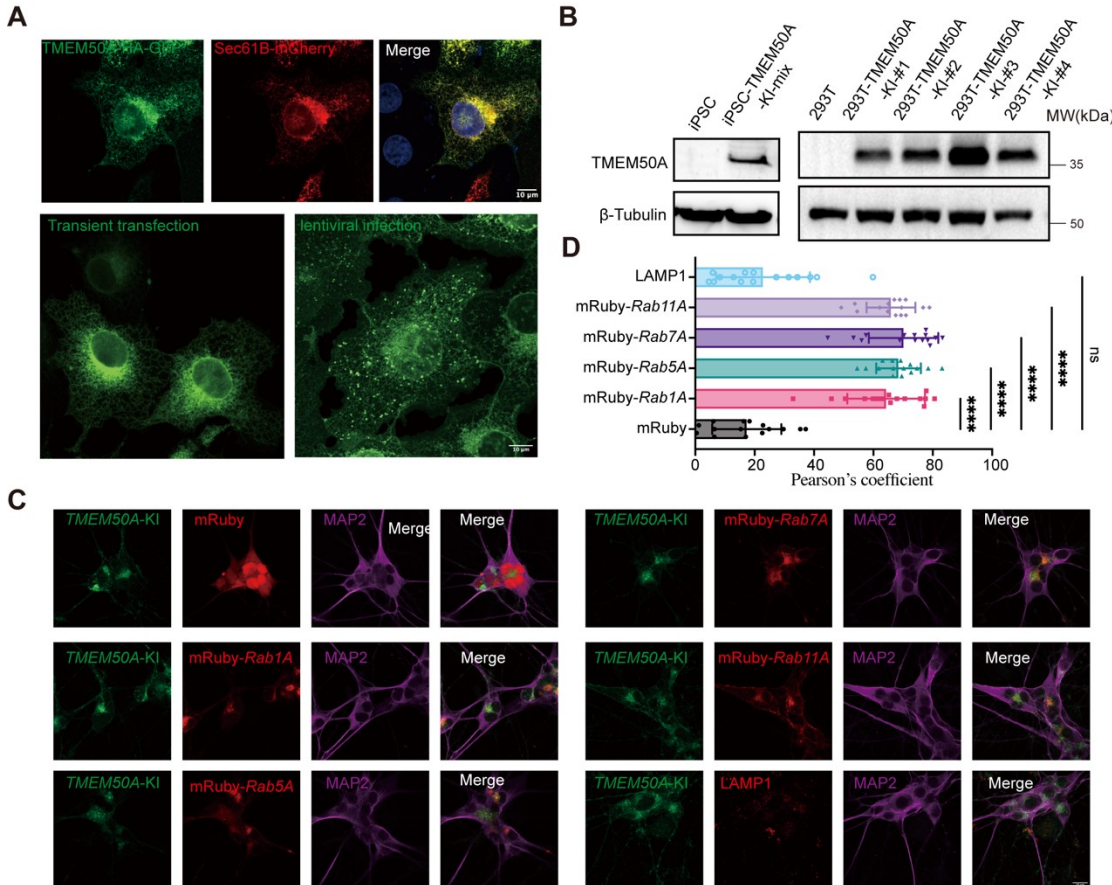
(A) RT-qPCR analysis of *TMEM50A* expression in WT and *TMEM50A* knockdown iNeurons. Data are shown as mean \pm SD (n = 3). ****p < 0.0001, one-way ANOVA.

(B). Representative phase-contrast images of WT and *TMEM50A* KO iNeurons at Day 21, showing comparable overall neuronal morphology. Scale bars, as indicated.

(C). Sanger sequencing of WT and *TMEM50A* KO iNeurons confirming the genetic knockout in two independent clones (KO#1 and KO#2).

135

1613



1614

Figure S3. TMEM50A localizes to endosomal compartments but not lysosomes

(A) Localization of exogenously expressed *TMEM50A* is affected by its overexpression levels. transient transfection produces prominent ER/reticular localization (top and bottom left), whereas lower-level lentiviral expression reveals predominantly punctate/vesicular *TMEM50A* distribution (bottom right). Scale bars, 10 μm.

(B) Western blot validation of *TMEM50A*-3×FLAG-mNeonGreen KI in hiPSCs and HEK293T cells with anti-Flag antibody.

(C) Representative immunofluorescence images of *TMEM50A*-KI iNeurons (green) with endosomal and lysosomal markers as indicated (red) and stained for MAP2 (purple). Scale bar, 10 μm.

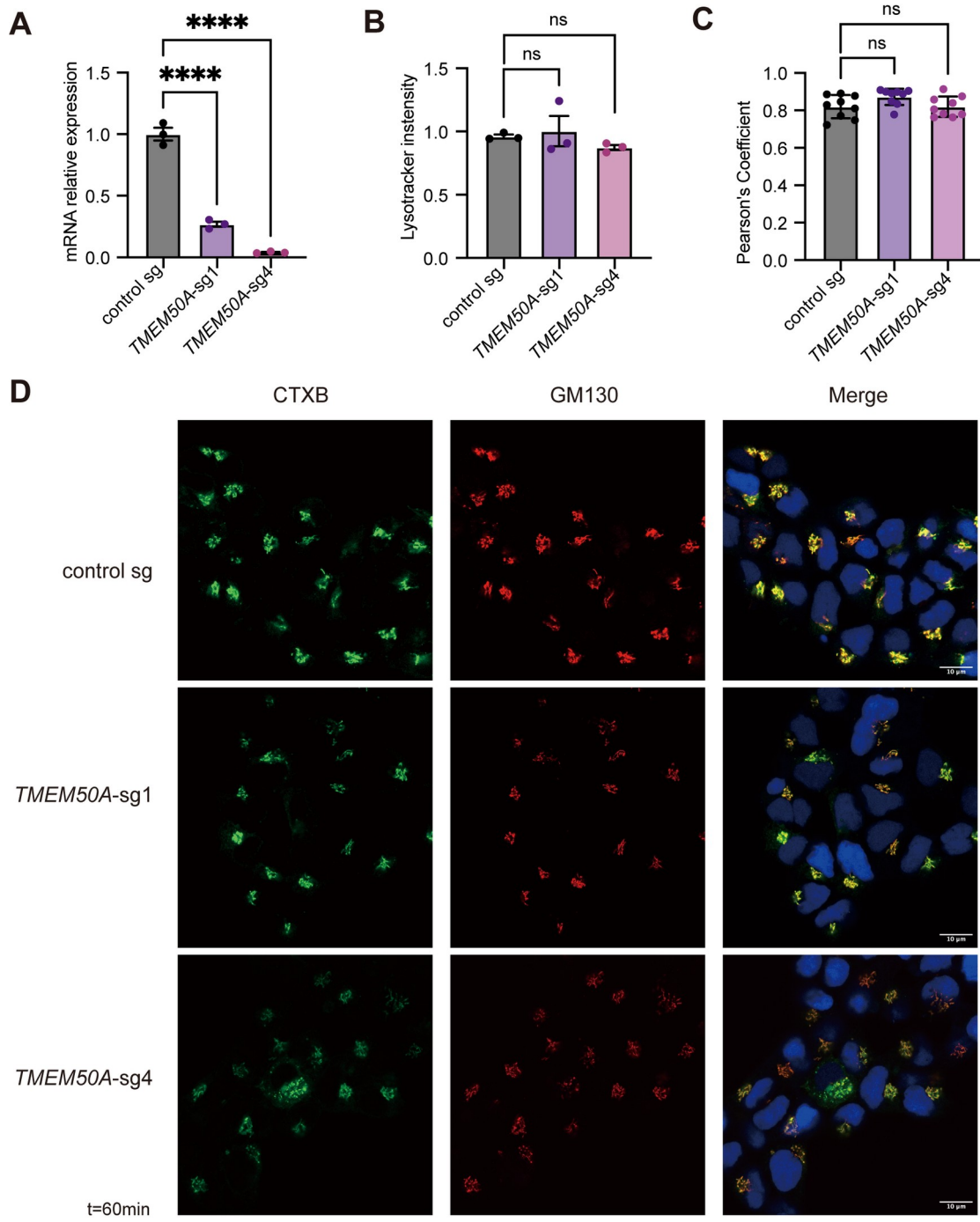
(D) Quantification of co-localization between *TMEM50A*-KI and

136

137

1628 indicated compartment markers using Pearson's correlation
1629 coefficient. Data are shown as mean \pm SD (n = 15 imaging fields). ns,
1630 not significant. ***p < 0.0001, one-way ANOVA.

138



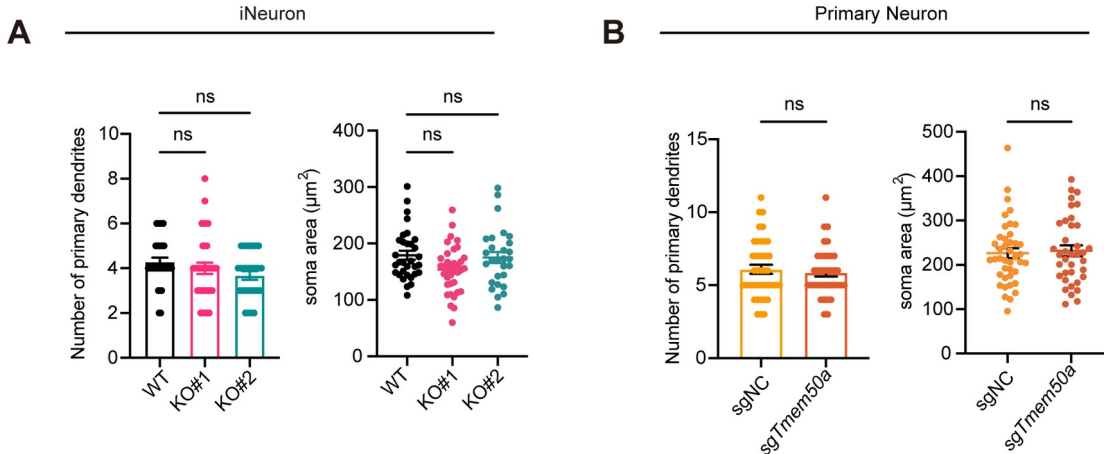
1632 **Figure S4. *TMEM50A* knockdown does not disrupt lysosomal
1633 integrity or retrograde transport**

1634 (A) qRT-PCR analysis confirming efficient *TMEM50A* knockdown in
1635 HEK293T cells expressing two independent *TMEM50A*-targeting
1636 sgRNAs (*TMEM50A-sg1*, *TMEM50A-sg4*) compared with control
1637 sgRNA. Data are presented as mean \pm SD (n = 3 technical

141

1638 replicates). ****p < 0.0001, one-way ANOVA.
1639 (B) Quantification of Lysotracker fluorescence intensity in control
1640 and *TMEM50A*-knockdown HEK293T cells. Data are mean \pm SD (n =
1641 3 technical replicates). ns, not significant, one-way ANOVA.
1642 (C) Quantification of the Pearson's correlation coefficient measuring
1643 colocalization of GM130 and CTxB. Data are mean \pm SD (n = 8
1644 imaging fields). ns, not significant, one-way ANOVA.
1645 (D) Representative confocal images of CTxB (green) and GM130
1646 (red) in control and *TMEM50A*-knockdown HEK293T cells after a
1647 60-min chase, with nuclei stained by DAPI (blue). Scale bar, 10 μ m.
1648

142



1649

1650 **Figure S5. TMEM50A loss does not affect neuronal**
1651 **morphology**

1652 Quantifications of number of primary dendrites and soma area in
1653 iNeurons (A) (WT n=32, KO#1 n=36, KO#2 n=28, ns, not
1654 significant, one-way ANOVA) and primary mouse neurons (B) (sgNC
1655 n=41, sg *Tmem50a*=37, ns, not significant, unpaired t test). Data
1656 was analysed using same confocal images from Figure 5&6.

1657

145

1658 **Supplementary Materials**

1659 Table S1: sgRNA protospacer sequences for the memory-associated
1660 gene library

1661 Table S2: sgRNA counts and MAGeCK-iNC analysis results from the
1662 CaMPARI2-CRISPRi screen

1663 Table S3: sgRNA and primer sequences used in this study

1664 Table S4: TMEM50A interactome identified by IP-MS

1665 Table S5: Surface proteome comparing TMEM50A KO and WT
1666 iNeurons

1667

146